Coarse Graining Molecular Dynamics with Graph Neural Networks

Brooke E. Husic, $^{1,2,a)}$ Nicholas E. Charron, $^{3,4,b)}$ Dominik Lemm, $^{5,b)}$ Jiang Wang, 4,6 Adrià Pérez, 5 Andreas Krämer, 1 Yaoyi Chen, 1,7 Simon Olsson, 1 Gianni de Fabritiis, $^{5,8,c)}$ Frank Noé, $^{1,4,6,9,d)}$ and Cecilia Clementi, $^{9,3,4,6,e)}$

- ¹⁾Department of Mathematics and Computer Science, Freie Universität, Berlin, Germany
- ²⁾ Department of Chemistry, Stanford University, Stanford, CA, USA
- ³⁾ Department of Physics, Rice University, Houston, TX, USA
- ⁴⁾ Center for Theoretical Biological Physics, Rice University, Houston, TX, USA
- ⁵⁾Computational Science Laboratory, Universitat Pompeu Fabra, PRBB, C/Dr Aiguader 88, Barcelona, Spain
- ⁶⁾Department of Chemistry, Rice University, Houston, TX, USA
- ⁷⁾ IMPRS-BAC, Max Planck Institute for Molecular Genetics, Berlin, Germany
- ⁸⁾ Institucio Catalana de Recerca i Estudis Avanats (ICREA), Passeig Lluis Companys 23, Barcelona, Spain
- 9) Department of Physics, Freie Universität, Berlin, Germany

Coarse graining enables the investigation of molecular dynamics for larger systems and at longer timescales than is possible at atomic resolution. However, a coarse graining model must be formulated such that the conclusions we draw from it are consistent with the conclusions we would draw from a model at a finer level of detail. It has been proven that a force matching scheme defines a thermodynamically consistent coarse-grained model for an atomistic system in the variational limit. Wang et al. [ACS Cent. Sci. 5, 755 (2019)] demonstrated that the existence of such a variational limit enables the use of a supervised machine learning framework to generate a coarse-grained force field, which can then be used for simulation in the coarse-grained space. Their framework, however, requires the manual input of molecular features upon which to machine learn the force field. In the present contribution, we build upon the advance of Wang et al. and introduce a hybrid architecture for the machine learning of coarse-grained force fields that learns their own features via a subnetwork that leverages continuous filter convolutions on a graph neural network architecture. We demonstrate that this framework succeeds at reproducing the thermodynamics for small biomolecular systems. Since the learned molecular representations are inherently transferable, the architecture presented here sets the stage for the development of machine-learned, coarse-grained force fields that are transferable across molecular systems.

I. INTRODUCTION

Technologies facilitating molecular dynamics (MD) simulations, such as distributed computing^{1–3} and bespoke hardware⁴, have made great strides in terms of the time- and length-scales accessible *in silico*. However, even the longest protein simulations still fail to reach total times exceeding milliseconds, and dedicated analysis methods are required to infer dynamics at longer timescales^{5,6}. In the context of such limitations at full atomistic resolution, coarse graining provides a crucial methodology to more efficiently simulate and analyze biomolecular systems. In addition to the practical advantages that arise from more efficient sampling, coarse graining can also elucidate the physical components that play key roles in molecular processes.

Coarse graining is especially useful for analyzing structures and processes that reach beyond the length- and time scales accessible to all-atom MD. Important examples include protein folding, protein structure prediction, and protein interactions⁷. Some of the most-used coarse-grained models for such studies are structure-based models⁸, MARTINI^{9,10}, CABS¹¹, AWSEM¹², and Rosetta¹³. These models differ with respect to their potential energy function, parameterization approaches, and resolution, which in combination determine their efficiency, accuracy, and transferability. In the past decade, coarse-grained models have become increasingly powerful due to an unprecedented wealth of experimental reference data and computational capabilities. In this context, the development of more realistic architectures and modeling approaches is of prime importance.

Here, we consider coarse graining to be the process of reducing structural degrees of freedom to facilitate more efficient simulation with specific goals in mind (e.g., reproducing system thermodynamics). Coarse graining can be implemented with a "top down" or "bottom up" approach, although other categories can be determined and strategies can be combined¹⁴. In a "top down" scheme, coarse graining frameworks are explicitly designed to reproduce certain macroscale emergent properties¹⁴. In a "bottom up" framework, which we consider here, implementations focus instead on reproducing specific features from a more detailed model.

The latter involves (i) a mapping from the entities in a fine-grained (e.g., atomistic) representation to a smaller set of interaction sites, often called "beads," and (ii) a physical model (i.e., Hamiltonian function) for the

a) Electronic mail: bhusic@fu-berlin.de; B.E.H., N.E.C., and D.L. contributed equally to this work.

b)B.E.H., N.E.C., and D.L. contributed equally to this work.

c) Electronic mail: gianni.defabritiis@upf.edu

d) Electronic mail: frank.noe@fu-berlin.de

e) Electronic mail: cecilia.clementi@fu-berlin.de

coarse-grained system comprising those beads. Good choices for the mapping and model will lead to more efficient simulation while preserving the biophysical properties of interest to the researcher. Modern machine learning techniques have been recently employed to learn both the mapping 15,16 and the model $^{17-20}$ components of bottom up coarse graining.

In the present contribution, we focus on the coarse graining model and employ a bottom up "force matching" scheme formulated as a supervised machine learning problem to reproduce the thermodynamics of small biomolecular systems. Particularly, we modify the architecture of the recently-introduced CGnet framework 19 such that the molecular features it requires are learned instead of hand-selected as in the original formulation. By leveraging the inherently transferable SchNet scheme 21,22 to learn features, we render the entire CGnet framework transferable across molecular systems.

Our goal in this paper is to present the theory underlying CGSchNet—our new transferable coarse graining architecture—and to demonstrate its success on learning the thermodynamics of individual biomolecular systems. We find that our new protocol produces more accurate free energy surfaces in comparison with the use of hand-selected features, is more robust to hyperparameter choices, and requires less regularization. Presented alongside a machine learning software package that implements the methods introduced, the current contribution sets out a framework for the machine learning of transferable, coarse-grained molecular force fields and demonstrates its application to a small peptide system and the miniprotein chignolin²³. The practical application of the methods described herein to larger protein systems, particularly those characterized by meaningful tertiary structure, remains an open challenge that will be explored in future work.

II. THEORY

The force matching technique, described in detail below, has been employed in two different contexts. Force matching was pioneered in the atomistic setting, in which forces obtained from an inexpensive calculation are matched to forces computed at a more computationally expensive level of theory (i.e., quantum) via an optimization scheme²⁴. Force matching was later adapted by the coarse graining community; in that context, coarsegrained representations are sought such that the forces computed from the coarse-grained energy function for a given configuration match the average forces on corresponding atomistic representations²⁵.

However, the underlying motivations in the two contexts differ. Because coarse graining away degrees of freedom entails that multiple atomistic structures will correspond to the same coarse-grained configuration, it is impossible to obtain zero error during force matching in the coarse graining context. We will see, however, that it can

be proven that the coarse graining model that matches the *mean* forces yields the correct thermodynamics. The corresponding force matching procedure minimizes the same objective as in the atomistic case, but that objective is now variationally bounded from below by a value that necessarily exceeds zero.

In the following sections, we overview the major advances that enable the present contribution; namely, the initial formulation of force matching in the atomistic context by Ercolessi and Adams 24 (Sec. II A); the adaptation of force matching to the multiscale problem of coarse graining by Izvekov and Voth 25 (Sec. II B); the formalization of the associated variational principle by Noid et al. 26 (Sec. II C); and, finally, CGnets: the fashioning of force matching as a supervised machine learning problem by Wang et al. 19 (Sec. II D).

The practically inclined reader may proceed directly to Sec. III, where we discuss the CGnet architecture and introduce this work's methodological contribution: namely, the incorporation of learnable molecular features into CGnet via the use of continuous filter convolutions on a graph neural network (i.e., SchNet^{21,22}). We will see in Sec. III that the scheme we introduce here enables, at least in principle, for the first time, a fully transferable coarse graining architecture. The practical use of this architecture to learn a force field in a transferable context will be addressed in future work.

A. Force matching at atomic resolution

Consider an all-atom dataset of coordinates and corresponding forces which we have obtained using a high level calculation (e.g., ab initio). We denote each three-dimensional structure $\mathbf{r}_i \in \mathbb{R}^{3N}, i = 1, ..., M$, and the forces $\mathbf{F}(\mathbf{r}_i) \in \mathbb{R}^{3N}$, where N is the number of atoms in the system. Now consider a trial energy function $\hat{V}(\mathbf{r}_i; \boldsymbol{\Theta})$, which takes as arguments an atomistic configuration \mathbf{r}_i and any parameters $\boldsymbol{\Theta}$. We would like to use \hat{V} to predict the forces on every \mathbf{r}_i —presumably in a more efficient way—by taking its negative derivative. We can write the "force matching" problem of comparing the two sets of atomistic forces as,

$$L(\mathbf{R}; \boldsymbol{\Theta}) = \frac{1}{3MN} \sum_{i=1}^{M} \| \underbrace{\mathbf{F}(\mathbf{r}_i)}_{\text{"True"}} + \underbrace{\nabla_{\mathbf{r}_i} \hat{V}(\mathbf{r}_i; \boldsymbol{\Theta})}_{\text{(Negative)}} \|^2, \quad (1)$$

where ${f R}$ is the set of all M sampled atomistic configurations.

The objective (1) was introduced by Ercolessi and Adams to analyze *ab initio* simulations of elemental aluminum²⁴. The authors focused specifically on using atomistic forces calculated from first principles to produce interatomic potentials numerically, as opposed to modeling potentials with complicated analytical expressions.

Ercolessi and Adams raise three crucial points with respect to their force matching procedure²⁴. First, they highlight the need to accommodate invariant properties of the system (in this case, they maintained adherance to glue potential equations for aluminum). Second, they discuss the transferability of a potential approximated by force matching; in particular, they note the need for a variety of geometries, physical conditions, and system identities in **R** if the learned potential is to be transferable across conformation, thermodynamic, or chemical space, respectively. Finally, the authors note that the "computational engine" of the force matching problem is the minimization procedure required to optimize (1), e.g. in the presence of multiple local minima²⁴.

A decade later, Izvekov et al. introduced a new force matching methodology inspired by the work of Ercolessi and Adams but applicable to more complex systems²⁷. The contribution's key advance addresses the third point above: instead of using numerical minimization to obtain an optimal but nonunique parameter set (e.g., via simulated annealing), Izvekov et al. fashion an overdetermined linear system that yields a unique parameter set Θ , increasing the framework's tractability for more complex systems. The authors showcase their method on Car-Parrinello MD simulations of liquid water and find good agreement with the original data for long-timescale processes such as diffusion²⁷. A recent review also presents an analytical method for determining the coarse-grained potential for polymeric liquids in the context of concerns of accuracy, transferability, and computational efficiency 28 .

B. Force matching as a coarse graining algorithm

In two follow-up papers, Izvekov and Voth present the groundbreaking advance of using force matching in the context of coarse graining ^{25,29}. They introduce the multiscale coarse graining (MS–CG) method and apply it to a lipid bilayer model. The MS–CG framework involves two steps: first, atoms are aggregated into "interaction sites," and second, force matching is performed between a transformation of the atomistic forces and a set of predicted coarse-grained forces. This procedure thereby creates a "multiscale" link between the all-atom and coarse-grained representations²⁵.

To understand the force matching framework for coarse graining, we require some additional notation. A linear coarse-grained mapping from N atoms to n interaction sites (henceforth "beads") takes the form,

$$\mathbf{x}_i = \mathbf{\Xi} \mathbf{r}_i \in \mathbb{R}^{3n},\tag{2}$$

where \mathbf{x}_i is the coarse-grained representation with n < N beads and the matrix $\mathbf{\Xi} \in \mathbb{R}^{3n \times 3N}$ effectively performs a clustering from the original atoms to the beads.

In this context, we consider a coarse-grained energy

function $U(\mathbf{x}; \boldsymbol{\Theta})$. Let's say we have a set of M coarse-grained configurations that we have obtained by applying (2) to every configuration $\mathbf{r}_i \in \mathbf{R}$. To calculate the forces on the beads, we then take the negative derivative of U with respect to the reduced coordinates; in other words, we evaluate,

$$-\nabla U(\mathbf{\Xi}\mathbf{r}_i; \mathbf{\Theta}) = -\nabla_{\mathbf{x}_i} U(\mathbf{x}_i; \mathbf{\Theta}) \in \mathbb{R}^{3n},$$

for each configuration i. From here we have all the ingredients to write down the adaptation of (1) to the MS–CG method:

$$L(\mathbf{R}; \mathbf{\Theta}) = \frac{1}{3Mn} \sum_{i=1}^{M} \| \underbrace{\mathbf{\Xi}_{\mathbf{F}} \mathbf{F}(\mathbf{r}_i)}_{\text{Atomistic forces mapped to coarse-grained space}} + \underbrace{\nabla U(\mathbf{\Xi} \mathbf{r}_i; \mathbf{\Theta})}_{\text{(Negative) forces predicted from coarse-grained model}} \|^2.$$
(3)

where $\Xi_{\mathbf{F}}\mathbf{F}$ is the *instantaneous* coarse-grained force (also called the *local mean force*); that is, the projection of the atomistic force into the coarse-grained space. A general expression for the force projection³⁰ is $\Xi_{\mathbf{F}} = (\Xi\Xi^{\top})^{-1}\Xi$. However, other choices for the mapping $\Xi_{\mathbf{F}}$ are possible and used for coarse-graining²⁶.

In principle, the coarse graining energy $U(\mathbf{x})$ that is exactly thermodynamically consistent with the atomistic energy $V(\mathbf{r})$ can be expressed analytically as:

$$U(\mathbf{x}) = -k_B T \ln p^{\text{CG}}(\mathbf{x}) + \text{Constant},$$
 (4)

where k_B is Boltzmann's constant and T is the absolute temperature. The function $p^{\rm CG}$ is the marginal probability density,

$$p^{\text{CG}}(\mathbf{x}') = \frac{\int_{\mathcal{R}} \exp\left(-\frac{V(\mathbf{r})}{k_B T}\right) \delta(\mathbf{x}' - \mathbf{\Xi}\mathbf{r}) d\mathbf{r}}{\int_{\mathcal{R}} \exp\left(-\frac{V(\mathbf{r})}{k_B T}\right) d\mathbf{r}}, \quad (5)$$

where \mathcal{R} is the set of all possible atomistic configurations. Since we are concerned with all theoretically accessible structures and (thus) employ an integral formulation, we have dropped the subscripts i with the understanding that \mathbf{x}' and \mathbf{r} now refer to infinitesimally small regions of their respective configuration spaces. \mathbf{x}' is distinguished from \mathbf{x} to emphasize that (5) is substituted into (4) as a function, not a number.

The coarse-grained energy function (4) is called the potential of mean force (PMF) and is an analogue of the atomistic potential energy function. Via (5), it is a function of weighted averages of energies of atomistic configurations. For a given coarse-grained structure \mathbf{x}' , in (5) we evaluate whether every possible $\mathbf{r} \in \mathcal{R}$ maps to \mathbf{x}' . We expect multiple atomistic configurations \mathbf{r} to map to \mathbf{x}' due to the reduction in degrees of freedom that

results from structural coarse graining (n.b., this means the PMF is in fact a free energy, as it contains entropic information 14). In these cases, the Dirac delta function in (5) returns one, and the contribution of that atomistic configuration to the marginal probability distribution is a function of its Boltzmann factor. If \mathbf{r} does not map to \mathbf{x}' , then the evaluation of the delta function (and thus the contribution of that atomistic structure to the free energy of \mathbf{x}') is zero. The denominator of the right-hand side of (5) is the all-atom partition function, which serves as a normalization factor.

To calculate the forces on our coarse-grained beads, we must take the gradient of (4). However, since we cannot exhaustively sample \mathcal{R} , (5) is intractable, and we must approximate U instead. One way to approximate U is to employ force matching—that is, by minimizing expression 3—as we describe in Sec. II D. Another method, which we do not discuss in this report, is through relative entropy³¹, whose objective is related to that of force matching^{14,32}.

C. Quantitative guarantees and the variational method

Before we describe our approximation of U, however, we must establish some mathematical implications of the force matching framework. In a report that generalizes the earlier work of Izvekov and Voth^{25,29}, Noid *et al.* set forth a theoretical architecture for the MS–CG method and expose its underlying variational principle²⁶. Crucially, they formalize the notion of thermodynamic consistency and establish the conditions under which it is guaranteed by the MS–CG approach.

Noid et al. define consistency in configuration space (i.e., for positions only) as the fulfillment of two requirements: first, that the coarse-grained coordinates are a well-defined linear combination of the coordinates of the all-atom system (cf. (2)), and second, that the equilibrium distribution of the coarse-grained configurations is equal to the one implied by the equilibrium distribution of the atomic configurations (cf. (4)). We hence refer to the satisfaction of these requirements as thermodynamic consistency, which is accordant with the scope of MS–CG as described by Izvekov and Voth ²⁵ (i.e., that the method only yields thermodynamic information).

Noid et al. then prove that, given a linear mapping from atoms to coarse-grained beads, thermodynamic consistency can only be achieved if each bead has at least one atom that is "specific to" it; i.e., is exclusively a component of that and no other bead. The authors show the coarse-grained potential that achieves thermodynamic consistency at a given temperature is unique (up to an additive constant, cf. (5)). Finally, the authors consider a set of possible coarse-grained force fields (i.e. the derivatives of a set of functions of coarse-grained configurations), including the unique one that achieves thermodynamic consistency. They go on to define an error functional that is (uniquely) minimized for the thermo-

dynamically consistent coarse-grained force field, thereby expressing the variational principle underlying the MS–CG method²⁶. In theory, then, a variational method can be used to search for the consistent coarse-grained force field²⁶. In practice, such a search is limited by the basis of trial force fields as well as the finite simulation data used—this is further explored in a companion paper from the same authors³³.

This contribution from Noid et al. is crucial because it formally proves a notion that had only previously been implicitly assumed: namely, that a consistent coarse-grained model will yield the same thermodynamics as an all-atom model (at a given temperature) if it were possible to sufficiently sample the latter²⁶. Equipped with this formulation, we can proceed with the understanding that if our linear mapping Ξ obeys the correct restrictions (2) and (4), we can, in principle, variationally approach the thermodynamically consistent force field.

However, the variational framework is not in itself sufficient to address key challenges for bottom up methods¹⁴. For example, the accuracy of a variationally optimized model is dependent upon the suitability of the basis set of force fields from which the model is chosen. In other words, the variational method is only as good as the best of the available model candidates (as assessed by finite simulation data from those models). One important consideration in this regard is how and which multibody effects should be incorporated¹⁴; such a choice will restrict the basis set of possible models.

D. CGnet: coarse graining as a supervised machine learning problem

We can refer to (1) and (3) as "loss functions" because they return a scalar that assumes a minimum value on the optimal model. In a recent report from Wang *et al.*, this fact is leveraged to formulate coarse graining via force matching as a supervised machine learning problem¹⁹. The authors discuss how the aim of coarse graining is equivalent to that of a supervised machine learning task: i.e., to learn a model with minimal error on a new set of data points that were not used during training¹⁹.

Wang et al. present several crucial contributions in their study 19 . First, they decompose the error term implied by (3) into three components—bias, variance, and noise—that are physically meaningful in the context of the force field learning problem. The bias represents the expected discrepancy between the mean forces and the average force field predicted by the model, while the variance emerges from finite training data 19 . The remaining error is attributed to "noise," which arises due to the mapping of multiple atomistic configurations to the same coarse-grained structures (the noise is related to the so-called "mapping entropy" introduced by Foley, Shell, and Noid 34). Crucially, the noise depends only on the change of resolution; it is not affected by changes in parameters Θ , and is not expected to drop to zero 19,26 .

Second, the authors introduce CGnet: a neural network architecture designed to minimize the loss in (3). The input data comprises coarse-grained structures $\Xi \mathbf{r}_{i}$, while the output data "labels" are the mapped forces $\Xi_{\mathbf{F}}\mathbf{F}(\mathbf{r}_i)$. Once a CGnet is trained, it can be used as a force field for new data points in the coarse-grained space (see Sec. III A 7). Every transformation from the input to the output is designed to be differentiable (i.e., amenable to backpropagation), such that modern machine learning methods and software (e.g., PyTorch³⁵) can be used for learning the network parameters. Furthermore CGnets are designed to enforce known properties of the system, such as roto-translational invariances and equivariances ¹⁹ (recall that Ercolessi and Adams noted this requirement in their original presentation²⁴). The CGnet architecture is discussed in more detail in Sec. III.

Third, Wang et al. augment their initial CGnet framework to introduce regularized CGnets¹⁹. The authors discover that the naïve training scheme described above, in which coarse-grained forces are regressed on the corresponding atomistic data, produces "catastrophically wrong" predictions and simulation results. This outcome stems from the absence of training data in regions of configuration space that are not accessed by the atomistic system. Regularized CGnets avoid this problem by introducing the calculation of prior energy terms before training. This adjustment means that, instead of learning the forces directly, the neural network learns a correction to the prior terms in order to match the atomistic forces.

Using regularized CGnets (henceforth, we assume all CGnets are regularized) on two peptide systems, the authors demonstrated effective learning of coarse-grained force fields that could not be obtained with a few-body model approach¹⁹. It is from this baseline that we present further advances to the CGnet methodology; to describe our contribution we first require a discussion of the practical implementation of force matching with CGnets.

III. METHODS

The pioneering contribution of Izvekov and Voth ²⁵ was the realization that force matching could be employed to optimize a coarse-grained representation of atomistic data. CGnets leverage the variational principle subsequently proven by Noid *et al.* ²⁶ to formulate force matching as a supervised machine learning problem ¹⁹. The implementation of CGnets is discussed below in Sec. III A.

In the quantum community, supervised machine learning has been used to predict energies on small molecules through a variety of approaches $^{22,36-51}$. In particular, the SchNet architecture is based on the use of continuous filter convolutions and a graph neutral network 21,22 . SchNet is a scalable, transferable framework that employs neural networks and representation learning to predict the properties and behavior of small organic molecules. In the vein of the original force matching procedure of Ercolessi and Adams 24 , SchNet has also been

used to predict forces on atomic data from a quantum mechanical gold standard 22 .

In Sec. III B, we describe SchNet and introduce our adaptation of SchNet to the coarse graining problem by incorporating it into a CGnet to create a hybrid "CGSchNet" architecture. The original implementation of CGnet is not transferable across different systems due to its reliance on hand-selected structural features¹⁹. We recognized that SchNet could be leveraged as a subcomponent of CGnet in order to learn the features, thereby converting CGnet—i.e., force matching via supervised machine learning—to a fully transferable framework for the first time.

A. Original CGnet architecture

Here, we describe the implementation of the CGnet architecture introduced in Sec. IID in practice.

1. Obtaining training data from atomistic simulations

Our training data comprises an MD simulation that has already been performed and for which the atomistic forces have been retained or recomputed. Both the configurations and the forces are in \mathbb{R}^{3N} space for N atoms. We then determine our mapping matrix Ξ and use it to prepare our input data (coarse-grained structures) and labels (atomistic forces mapped to the coarse-grained space), which will both be in \mathbb{R}^{3n} for n beads (recall (2)).

While the mapping is permitted to be more general (see also Sec. II C), in our work we restrict it to the special case where the matrix Ξ contains zeroes and ones only. With this choice of mapping, the projection of the forces in (1) becomes simply $\Xi_{\mathbf{F}} = \Xi$. Our mapping thus "slices" the original atomic configuration such that the corresponding coarse-grained representation comprises a subset of the original atoms. For example, a useful mapping might retain only protein backbone atoms or α -carbons.

2. Converting structures to features

We understand from physics that the coarse-grained energy will be invariant to the global translation or rotation of the input coordinates in space, and that the coarse-grained forces will be invariant to translation and equivariant under rotation.* Therefore, we choose to preprocess our "raw" structural data such that it is represented by features with the desired properties. A

^{*} In certain cases we also must enforce permutational invariance; since we only study peptides in the present contribution, we do not need to consider this here.

straightforward way to featurize the input data is to convert the spatial coordinates of the beads into a set of pairwise distances^{19,21}. The original CGnet architecture presented by Wang *et al.* also includes trigonometric transformations of planar (three-bead) and torsional (four-bead) angles among adjacent beads¹⁹. In the present work, on the other hand, instead of using hand-selected structural features, we require only distances and bead identities from which features are *learned*; this is described in Sec. III B.

3. Calculating prior terms

In a nonregularized CGnet, a neural network directly regresses the atomistic forces upon the input data by learning an energy term and then evaluating its derivative. This was observed to generate huge errors during prediction due to the (expected) absence of training data points for configurations not physically accessible ¹⁹. In a so-called "regularized CGnet", on the other hand, a prior energy term is calculated from the training data, providing a baseline energy for all of configuration space. The neural network component then learns corrections to the prior energy; from this corrected energy the forces are obtained.

Wang et al. use up to two types of prior terms in CGnets¹⁹. The first is a harmonic prior on selected distances (i.e., bonds or pseudobonds) and angles. The second is a repulsion prior that can be used on nonbonded distances. Respectively, these priors are defined as follows for a given feature f_i calculated from the data (e.g., a particular distance),

$$U_i^{\text{harmonic}}(f_i) = \frac{k_B T}{2 \text{Var}[f_i]} (f_i - \mathbb{E}[f_i])^2, \qquad (6a)$$

$$U_i^{\text{repulsion}}(f_i) = \left(\frac{\sigma}{f_i}\right)^c.$$
 (6b)

The constants in (6b) can be determined through cross-validated hyperparameter optimization as in Ref. 19.

The prior energy is the sum of each prior term for all relevant features f_i . In principle, any scalar function of protein coordinates can be used to construct a prior energy term.

4. Building the neural network

Once we have featurized our data and computed a prior energy, we must construct a neural network to learn corrections to the latter. For a CGnet as originally described 19 , we use a fully connected network (e.g., the optimal parameters for one of the peptide models in Wang et al. had 5 layers and 160 neurons). Wang et al. used the hyperbolic tangent to facilitate nonlinear transformations between the layers. L₂ Lipschitz regularization was

also employed 52 .

Crucially, the last layer of the network returns a scalar output. Because of this single node bottleneck structure, the resulting coarse-grained force field will be curl-free and is therefore guaranteed to conserve energy^{19,41}.

5. Training the model

So far, we have converted our raw simulation data to a coarse-grained mapping, featurized the mapped coordinates to accommodate physical symmetries, calculated a (scalar) prior energy term, and constructed a (scalar) neural network correction to the prior. These two scalars are summed to produce an estimated energy.

Since all the steps described are differentiable, we can use an autodifferentiation framework such as PyTorch³⁵ to take the derivative of the energy with respect to the original (coarse-grained) spatial coordinates via backpropagation. This derivative corresponds to the predicted forces on the coarse-grained beads in \mathbb{R}^{3n} , which can then be compared to the known forces on the training coordinates. The CGnet thereby identifies the free energy whose negative derivative most accurately approximates the forces in the training set¹⁹.

The neural network weights and other parameters are obtained through a training process involving stochastic gradient descent and the Adam optimizer⁵³. The predicted forces are compared with the mapped atomistic forces using force matching (i.e., according to (3)).

6. Cross-validation and hyperparameter searching

Whereas parameters such as node weights are optimized during the training of an individual model, hyperparameters such as the neural network depth and number of nodes must be chosen by comparing separately trained models according to the value of the loss function (3) when training is complete. Hyperparameters are chosen based on neural network performance on test data over multiple cross-validation "folds." The hyperparameter optimization procedure we use in this study is detailed in Appendix B.

7. Simulation with a trained model

Once hyperparameters have been selected, the trained model can be used as a force field to simulate the system in the coarse-grained space. Specifically, Langevin dynamics^{54,55} are employed to propagate coarse-grained coordinates \mathbf{x}_t forward in time according to,

$$\frac{\Delta \Delta \mathbf{x}_t}{(\Delta t)^2} = -\frac{\nabla U(\mathbf{x}_t)}{\mathbf{M}} - \gamma \frac{\Delta \mathbf{x}_t}{\Delta t} + \sqrt{\frac{2k_b T \gamma}{\mathbf{M}}} \mathbf{W}(t), \quad (7)$$

where the diagonal matrix \mathbf{M} contains the bead masses, γ is a collision rate with units ps⁻¹, and $\mathbf{W}(t) \sim \mathcal{N}(0,1)$ is a stochastic Wiener process with units ps^{-\frac{1}{2}}.\(^{\frac{1}{2}}\) In this work, we use $\Delta t = 0.02$ ps.

A subset of Langevin dynamics are so-called "overdamped" Langevin dynamics, also referred to as Brownian motion. Overdamped Langevin dynamics lack inertia; i.e., $\Delta \Delta \mathbf{x}_t = 0$. After setting the acceleration to zero, dividing both sides by γ , and rearranging terms, (7) becomes,

$$\frac{\Delta \mathbf{x}_t}{\Delta t} = -\frac{D}{k_B T} \nabla U(\mathbf{x}_t) + \sqrt{2D} \mathbf{W}(t), \tag{8}$$

where $D \equiv k_B T/\mathbf{M}\gamma$. Although D contains a notion of mass, we note that propagating coarse-grained dynamics via (8) does not actually require bead masses, since the product $\mathbf{M}\gamma$ can be considered without separating its factors. Wang *et al.* ¹⁹ use exclusively (8) to simulate dynamics from CGnets.

In both formulations, the noise term is intended to indirectly model collisions—e.g., from and among solvent particles—that are not present in the coarse-grained coordinate space. Since Langevin dynamics depend only on the coordinates (and, unless overdamped, velocities) of the previous time step, these simulations can easily be run in parallel from a set of initial coordinates. The resulting coarse-grained simulation dataset can then be used for further analysis as we will show in Sec. IV.

B. Replacing structural features with graph neural networks

Wang et al. show¹⁹ that using the structural features described in Sec. III A 2 in a CGnet produces accurate machine-learned force fields for a low-dimensional potential energy surface, capped alanine, and the miniprotein chignolin²³. From the trained CGnets, further simulations on the same system are performed using overdamped Langevin dynamics (recall (8)) and produce free energy surfaces comparable with those obtained from the baseline all-atom simulations. The model architecture is found to be somewhat sensitive to various hyperparameters and required individual tuning for each system (see e.g. Fig. 5 in Wang et al. ¹⁹). Furthermore, a new system will in general require retraining because the feature size is fixed according to the system geometry (recall Sec. III A 2).

In the present contribution, we replace the fixed structural features employed in the original CGnet formulation (i.e., distances, angles, and torsions)¹⁹ with *learned*

features computed using continuous filter convolutions on a graph neural network – here SchNet 21,22). The SchNet architecture thereby becomes a subunit of CGnet with its own, separate neural network scheme; we refer to this hybrid architecture as CGSchNet. Below, we briefly summarize SchNet and refer the reader to the original papers for more details 21,22 . Then, we describe the incorporation of SchNet into CGnet to create CGSchNet.

1. SchNet overview

One key motivating factor for the original development of SchNet is that, unlike the images and videos that comprise the datasets for much of modern machine learning, molecular structures are not restricted to a regular grid. Therefore, Schütt $et\ al.$ introduced continuous-filter convolutions to analyze the structures of small molecules with the goal of predicting energies and forces according to a quantum mechanical gold standard²¹. This development builds upon previous work in predicting atomic properties directly from structural coordinates^{41,43,56}.

SchNet is a graph neural network where the nodes correspond to particles embedded in three-dimensional space and the convolutional filters depend on the interparticle distances in order to preserve invariances expected in the system²¹. While SchNet was originally used to predict quantum-chemical energies from atomistic representations of small molecules, we here employ it to learn a feature representation that replaces the hand-selected features in a CGnet for the purpose of predicting the coarse-grained energy on the coarse-grained bead coordinates \mathbf{x}_i .

As in other graph neural networks, SchNet learns feature vectors on the nodes (here, coarse-grained beads). The initial node features at the input are called node or bead embeddings ζ_i^0 , which here correspond to nuclear charges (capped alanine) or amino acid identities (chignolin). These bead embeddings are optimized during training. Crucially, this entails that SchNet learns a molecular representation, which avoids the common paradigm of fixed, heuristic feature representations.

Bead representations are updated in a series of socalled "interaction blocks." Each interaction block comprises beadwise linear updates, continuous convolutions, and a nonlinearity as follows^{21,22,57}:

$$\zeta_i^{(B,1)} = W^{(B,0)} \zeta_i^{(B,0)} + b^{(B,0)}, \tag{9a}$$

$$\zeta_i^{(B,2)} = \sum_j \zeta_j^{(B,1)} \circ \mathcal{W}^{(B,1)}(\mathbf{x}_j - \mathbf{x}_i), \qquad (9b)$$

$$\zeta_i^{(B,3)} = W^{(B,2)} \zeta_i^{(B,2)} + b^{(B,2)}, \tag{9c}$$

$$\zeta_i^{(B,4)} = f\left(\zeta_i^{(B,3)}\right) \tag{9d}$$

$$\zeta_i^{(B,5)} = W^{(B,4)} \zeta_i^{(B,4)} + b^{(B,4)},$$
 (9e)

where ζ_i are the bead representations, B is the block in-

[†] Two conventions are adopted here. First, "division" by the M matrix indicates left-multiplication by its inverse. Second, the units of the Wiener process are chosen for ease of computation. $\mathbf{W}(t)$ may be converted to another Wiener process that is instead included in the square root term with units ps⁻¹.

dex, and \circ is elementwise multiplication. Steps (9a), (9c), and (9e) represent simple linear transformations with weights W and biases b, which are learned during training.

In step (9b), a filter-generating neural network \mathcal{W} that maps $\mathbb{R}^3 \to \mathbb{R}^{\varphi}$ for φ filter dimensions is used to create a continuous filter from the interbead distances. This filter is applied to the bead representations ζ_i once per interaction block. The sum in (9b) is taken over every bead j within the neighborhood of bead i, which can be all other beads in the system or a subset thereof if a finite neighborhood is specified. In step (9d), the function f represents a nonlinear transformation of the bead representation ζ_i . While the original implementation of SchNet uses shifted softplus for f^{21} , we use the hyperbolic tangent instead.

Finally, each interaction block B performs a residual update of the previous bead representation as in ResNets^{57,58}. This iterative "additive refinement" step prevents gradient annihilation in deep networks:

$$\zeta_i^{(B+1,0)} = \zeta_i^{(B,0)} + \zeta_i^{(B,5)},$$
 (9f)

where in the B=1 case (i.e., the first block), the first term on the right-hand side are the bead embeddings ζ_i^0 .

In the original SchNet implementation, after the last additive refinement step a series of further transformations are performed to ultimately yield a scalar energy^{21,22}. In this work, we instead "cut" SchNet after step (9f) of the last interaction block and input these learned features into the fully connected neural network part of a CGnet (i.e., in place of hand-picked geometric features; see Sec. III B 2).

In (9b), W is convolved with the bead representations ζ_i , thereby integrating the information contained in pairwise distances into the representations. Stacks of blocks thus enable the modeling of complex interactions among multiple beads in the system²¹. Particle neighborhoods can be imposed such that only distances within a specified cutoff are used at each layer, which has favorable scaling properties due to the finite number of beads that can be contained within an arbitrary radius²².

The loss function for the original SchNet formulation includes a force-matching term similar to (1) as well as an energy-matching term, where the former is weighted much less than the latter in most applications²². SchNet has been used to predict small molecule properties, energies of formation, and local chemical potentials^{21,22}. Similarly to CGnet, SchNet was also used to create a machine-learned force field by predicting molecular forces on a small molecule and propagating them forward in time (Schütt *et al.* used path integral MD)—in this case, only the force matching loss was used²².

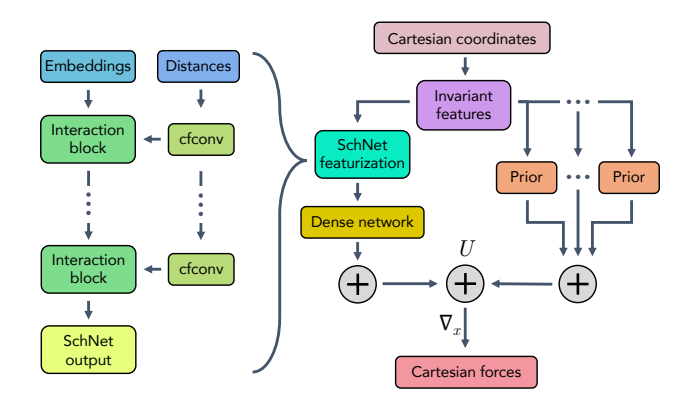


FIG. 1. CGSchNet architecture.

2. CGSchNet: a transferable architecture for coarse graining

Sections II and III A lay the groundwork for the advance we present here: namely, the incorporation of SchNet^{21,22} into CGnet. CGnet as originally presented is incapable of learning a transferable coarse-grained force field due to its reliance upon hand-picked structural features¹⁹. Since SchNet is inherently a transferable framework, learning CGnet features using SchNet enables the transferability of the entire CGnet architecture across molecular systems.

Our CGSchNet architecture is based on that of the original CGnet¹⁹, with the exception that instead of predetermined structural features—i.e., distances, angles, and torsions—a SchNet is used instead, enabling the model to learn the representation itself (see Fig. 1). By replacing fixed-size geometric features with SchNet, we obtain a more flexible representation that both scales better with system size and is amenable to a transferable architecture²². While angles and torsions may still be included in the prior energy terms, they are no longer propagated through any neural networks.

The use of SchNet requires us not only to provide structural coordinates but also a type for every bead. In the original (i.e., non-coarse graining) implementation for systems at atomic resolution, the types are atomic numbers^{21,22,43}. In the new context presented here (i.e., leveraging SchNet for coarse graining), we may specify coarse-grained bead types—effectively, chemical environments—however we deem appropriate for the system under study; for example, amino acid identities may be used.

Finally, we note that we retain the coarse-grained force matching loss (3) when comparing our predicted forces to the known forces from our training set. Unlike in the original SchNet formulation, we cannot straightforwardly incorporate an additional "energy matching" term into the coarse graining framework. This is because we have no estimate of the contribution of degrees of freedom that have been coarse grained out (e.g., solvent energies) or

their entropic contributions to the PMF (4).

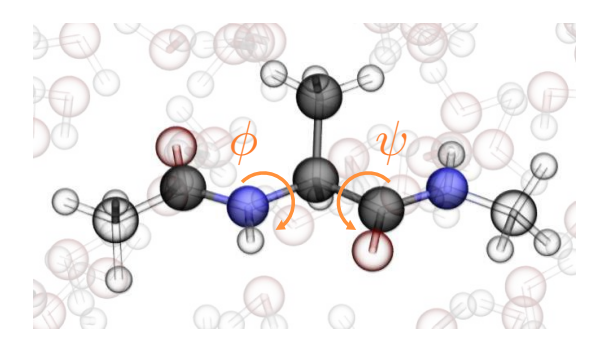


FIG. 2. Capped alanine in water. The six shaded atoms are the ones preserved in the coarse-grained representation. The ϕ and ψ dihedral angles completely describe the central alanine's heavy-atom dynamics.

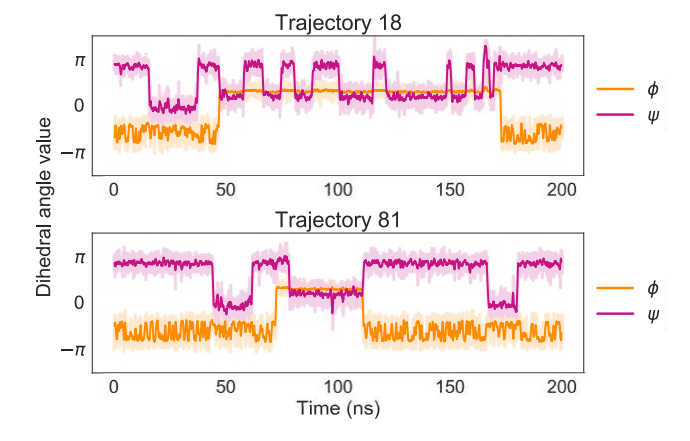


FIG. 3. Two 100-ns trajectories simulated using a CGSchNet trained on atomistic data of capped alanine. The orange and magenta lines represent the value of the dihedral angles ϕ and ψ , respectively, over the course of each simulation. Relatively steep changes in the y-direction indicate transitions among basins; one can see that both trajectories feature multiple transitions in both reaction coordinates. A moving average of 250 simulation frames is used to smooth the darker curves.

IV. RESULTS

A. Capped alanine

Capped alanine—often referred to alanine dipeptide for its two peptide bonds—is a common benchmark for MD methods development because the heavy-atom dynamics of the central alanine are completely described by the dihedral (torsional) angles ϕ and ψ (see Fig. 2). We performed a single 1- μ s all-atom, explicit solvent MD simulation for capped alanine and saved the forces to use for CGSchNet training (see Ref. 19 and Appendix A). We can visualize the occupancies of backbone angle conformations by creating a histogram of the data on ϕ ×

 ψ space and visualizing the populations of the histogram bins. This is called a Ramachandran map and is depicted in Fig. 4a for the atomistic simulation using a 60×60 regular spatial discretization.

As an initial benchmark of the CGSchNet method, we aim to learn a force field for a coarse-grained representation of capped alanine such that we can reproduce its heavy-atom dynamics using a trained CGSchNet instead of a more expensive explicit solvent all-atom MD simulation. For our coarse-grained mapping, we select the backbone heavy atoms $C-[N-C_{\alpha}-C]_{Ala}-N$ as well as the alanine C_{β} for a total of six beads.[‡] We use atomic numbers for the bead embeddings as in the original SchNet formulation²¹. A CGSchNet is trained on the coordinates and forces of the all-atom simulation depicted in Fig. 4a. The learning procedure involves a hyperparameter selection routine and the training of multiple models under five-fold cross-validation for each hyperparameter set (see Appendix B).

Once a final architecture has been selected, the trained model can serve as a force field in the coarse-grained space; i.e., by predicting the forces on a set of input coarse-grained coordinates. Along with an integrator, predicted forces can be used to propagate coarse-grained coordinates forward in time (recall Sec. IIIA7). This procedure (i.e., force prediction with CGSchNet followed by propagation with an integrator) is iterated until a simulation dataset of the desired duration has been obtained. Since we employ five-fold cross-validation during the model training procedure, we have five trained CGSchNet models with a common architecture at hand. To perform our coarse-grained simulation, we simultaneously predict the forces on each set of input coordinates from all five trained networks, and the mean force vector is used to propagate Langevin dynamics according to (7).

To facilitate sampling, 100 coarse-grained simulations of length 200 ns each are performed in parallel from various starting positions in Ramachandran space (see Appendix C and Fig. A3). The time series of the ϕ and ψ values for two of the trajectories that feature transitions among the major basins are plotted in Fig. 3. The same trajectories are also overlaid on the two-dimensional energy surface in Fig. A4.

Free energy surfaces resulting from the coarse-grained simulation dataset are presented in Fig. 4b. We can see qualitatively that the two-dimensional free energy surface from the CGSchNet simulation captures the same basins as the surface calculated from the baseline allatom simulation. In the one-dimensional free energy surfaces, we see that the barriers are well-approximated by the CGSchNet simulation data.

[‡] As in Ref. 20, we require the β -carbon in order to break the symmetry of the system (i.e., to enforce chirality). In their demonstration of CGnet, Wang *et al.* ¹⁹ used only the five backbone heavy atoms as beads because chirality is enforced through dihedral features, which we do not use here.

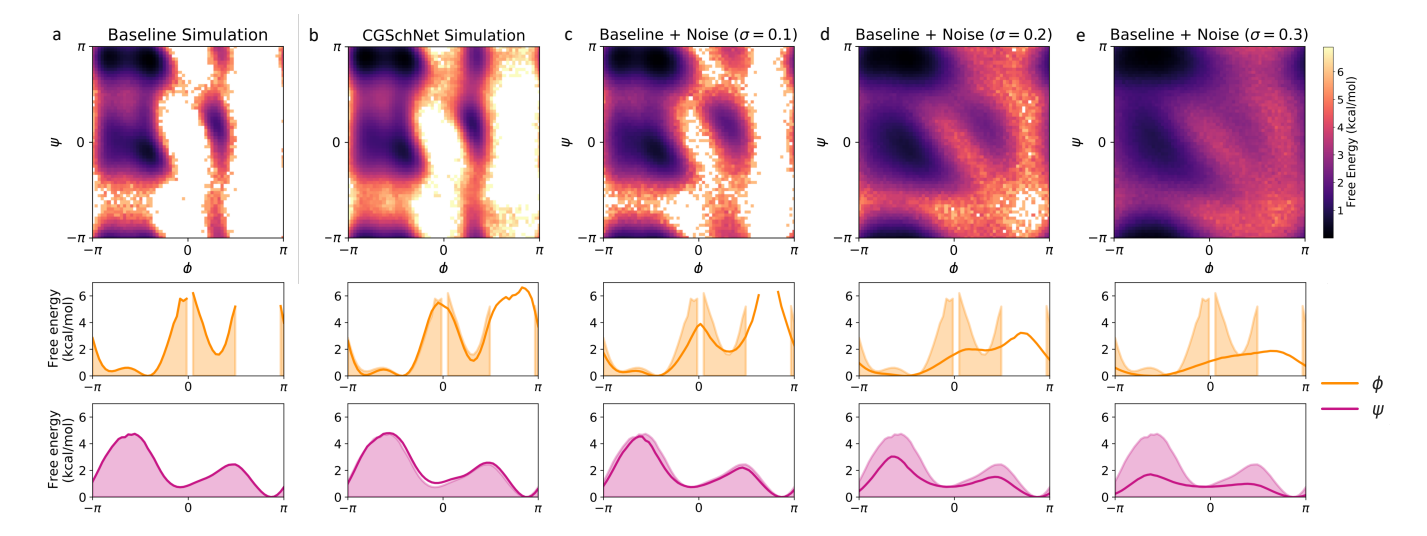


FIG. 4. Two- and one-dimensional free energy surfaces for five capped alanine datasets. From left to right, datasets are the baseline all-atom capped alanine simulation (a), the coarse-grained CGSchNet simulation produced for analysis (b), and datasets generated from perturbations of the original Cartesian coordinates of the baseline dataset drawn from noise distributed as $\sim \mathcal{N}(0, \sigma^2)$ for $\sigma = 0.1$ Å (c), 0.2 Å (d), and 0.3 Å (e). To create each two-dimensional surface, the ϕ and ψ Ramachandran angles are calculated from the spatial coordinates and discretized into 60×60 regularly spaced square bins. The bin counts are converted to free energies by taking the natural log of the counts and multiplying by $-k_BT$; the color scale is the same in all five two-dimensional surfaces and darker color represents lower free energy (i.e., greater stability). To obtain the one-dimensional ϕ and ψ landscapes, free energies are calculated for 60 regularly spaced bins along the reaction coordinate. The shaded region always represents the baseline dataset and the bold line represents the dataset indicated in the subfigure title.

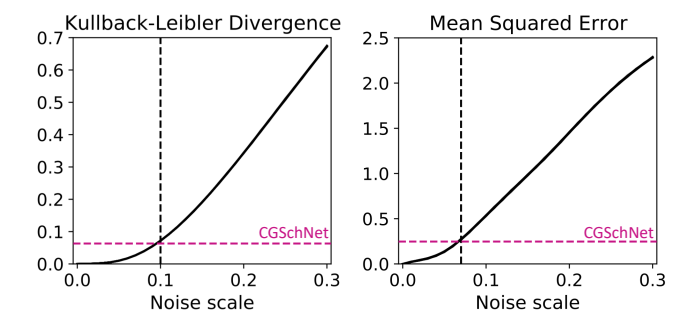


FIG. 5. The Kullback-Leibler divergence (left) and mean squared error (right) are calculated between the baseline dataset and the datasets obtained from perturbations to the baseline simulation at noise scale values of $\sigma \in \{0,0.01,0.02,\ldots,0.30\}$ where the former is the reference distribution and the latter is the trial distribution. This procedure is performed 50 times with different random seeds; both plots show the superposition of those 50 lines. The colored horizontal dashed line shows the value of the metric when comparing the CGSchNet simulation to the baseline and the black vertical dashed line indicates the noise scale σ that return the closest value for that metric. The KL divergence is computed for normalized bin counts in $\phi \times \psi$ space, and the MSE is computed for the energies of those bins as described in the main text.

To calibrate our understanding of the CGSchNet simulation dataset's relationship to the baseline atomistic simulation dataset, we create a set of new sys-

tems by perturbing the Cartesian coordinates of the latter with noise distributed as $\sim \mathcal{N}(0,\sigma^2)$ for $\sigma \in \{0,0.01,0.02,\ldots,0.30\}$ Å. From the perturbed Cartesian coordinates, the new ϕ and ψ dihedrals are calculated and assigned to the same 60×60 regularly spaced bins in Ramachandran space. Examples of the perturbed free energy surfaces are shown in Fig. 4c, d, and e for $\sigma = 0.1$ Å, 0.2 Å, and 0.3 Å, respectively. We see that the surfaces become smeared and the free energy barriers are reduced with increasing noise.

This ensemble of perturbed simulation datasets enables us to understand the CGSchNet-produced simulation in the context of the baseline atomistic simulation. To quantify the relationship between two distributions, we can use the Kullback-Leibler (KL) divergence⁵⁹ and a mean squared error (MSE) formulation. The KL divergence is defined for discrete distributions as,

$$-\sum_{i}^{m} p_i \ln \frac{q_i}{p_i}, \forall p_i \ge 0, \tag{10}$$

where p and q are the "reference" and "trial" distributions, respectively, and m is the number of bins in each discrete distribution. In this case, p and q represent the normalized bin counts. The index i returns the normalized count from the ith bin of a 60×60 regular discretization of $\phi \times \psi$ space. The distribution obtained from the baseline atomistic simulation always serves as the reference. The mean squared error used here is,

$$\frac{1}{m'} \sum_{i}^{m'} (P_i - Q_i)^2 \ni p_i q_i > 0, \tag{11}$$

where p_i and q_i remain the normalized bin counts and P_i and Q_i represent, respectively, the corresponding discrete distributions of bin energies calculated as, e.g., $P_i = k_B T \log p_i$ for Boltzmann's constant k_B and absolute temperature T. When no count is recorded for a bin in either p_i or q_i , those bins are omitted from the mean. m' represents the number of bins in which $p_i q_i > 0$ (i.e., both have finite energies). \S 50 different trials are performed at different random seeds for the full set of noise scales (i.e., at each noise scale for a given trial, values are drawn from $\mathcal{N}(0, \sigma^2) \in \mathbb{R}^{T \times 3n}$, where T is the length of the trajectory dataset and n is the number of coarse-grained beads). Within each trial, at each noise scale value σ , the KL divergence and MSE are calculated. The results are presented in the left plot in Fig. 5.

We see in Fig. 5 that as the noise increases, both divergence metrics also increase. The dashed lines in Fig. 5 show us that the error on the CGSchNet simulation dataset is approximately comparable to the corresponding error on the perturbed dataset with noise scale $\sigma=0.1$ Å (Fig. 4c) ¶. Upon qualitative comparison of the free energy surfaces, however, the former has more visual fidelity to the baseline surface in Fig. 4a than to the broader spread seen (and expected) in the latter. We know that coarse graining can result in increased population in transition regions that are rarely visited in an all-atom model; this is what we observe in Fig. 4b. As a corollary, we do not expect coarse graining to result in the absence of states known to exist in the baseline system.

B. Chignolin

The CLN025 variant of chignolin is a 10-amino acid miniprotein²³ featuring a β -hairpin turn in its folded state (Fig. 6). Due to its fast folding, its kinetics have been investigated in several MD studies^{60–65}. Our training data is obtained from an atomistic simulation of chignolin in explicit solvent for which we stored the forces (see Ref. 19 and Appendix A). To build our CGSchNet model, we retain only the ten α -carbons for our coarse-grained beads. For the SchNet embeddings, we assign each amino acid its own environment with a separate designation for the two terminal tyrosines. After determining hyperparameters for our CGSchNet model, we simulate chigno-

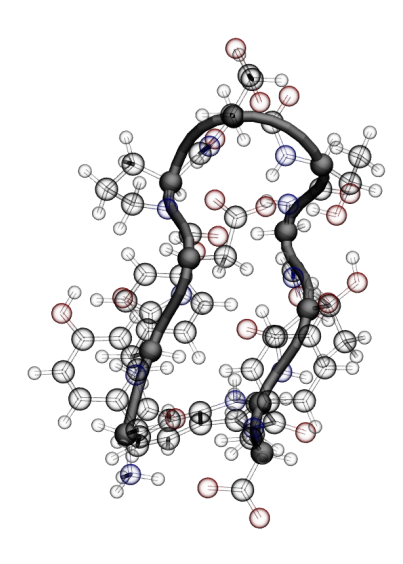


FIG. 6. The miniprotein chignolin. The α -carbon backbone is visualized in opaque black, and these ten atoms are the only beads preserved in the coarse-grained representation. The atomistic system is also solvated, although the water molecules are not shown here.

lin in the coarse-grained space using Langevin dynamics as in the previous section (7). The procedures for CGSchNet training and simulation are similar to those used for capped alanine and are described in Appendices B and C.

Given our CGSchNet simulation data, we are interested not only in performing a similar analysis to the one in the previous section for alanine dipeptide (i.e., comparison to the baseline dataset with and without noise added) but also to simulation data obtained from a CGnet trained according to the protocol in Ref. 19 for the same system. We thus also construct a CGnet (i.e., using fixed geometric features as described in Sec. III A) according to the parameters selected in Ref. 19 (see also Appendix B). Then, we create a simulation dataset using the protocol described in the previous section Appendix C. Finally, we employ a similar protocol to the previous section by perturbing the raw Cartesian coordinates of the all-atom chignolin simulation dataset with noise distributed as $\sim \mathcal{N}(0, \sigma^2)$ for $\sigma \in \{0, 0.03, 0.06, \dots, 0.90\}$ Å.

For each type of system (i.e., baseline, CGSchNet, CGnet, and baseline with noise perturbation), we build Markov state models (MSMs)⁶⁶. First, the data is "featurized" from Cartesian coordinates into the set of 45 distances between pairs of α -carbons. From these distances, TICA^{67,68} is performed to yield four slow reaction coordinates for the system. These four reaction coordinates are clustered into 150 discrete, disjoint states using the k-means algorithm. An MSM is then estimated from the cluster assignments. The MSM for the baseline simulation dataset is constructed first; then, the other simulation datasets are projected onto the space defined by the former. MSM essentials are presented in Appendix D from a theoretical standpoint, and the specific protocols

 $[\]S$ We could alternatively compute the mean squared error between discrete distributions of counts without omitting any bins.

[¶] Similar results were obtained for the two-dimensional Wasserstein distance.

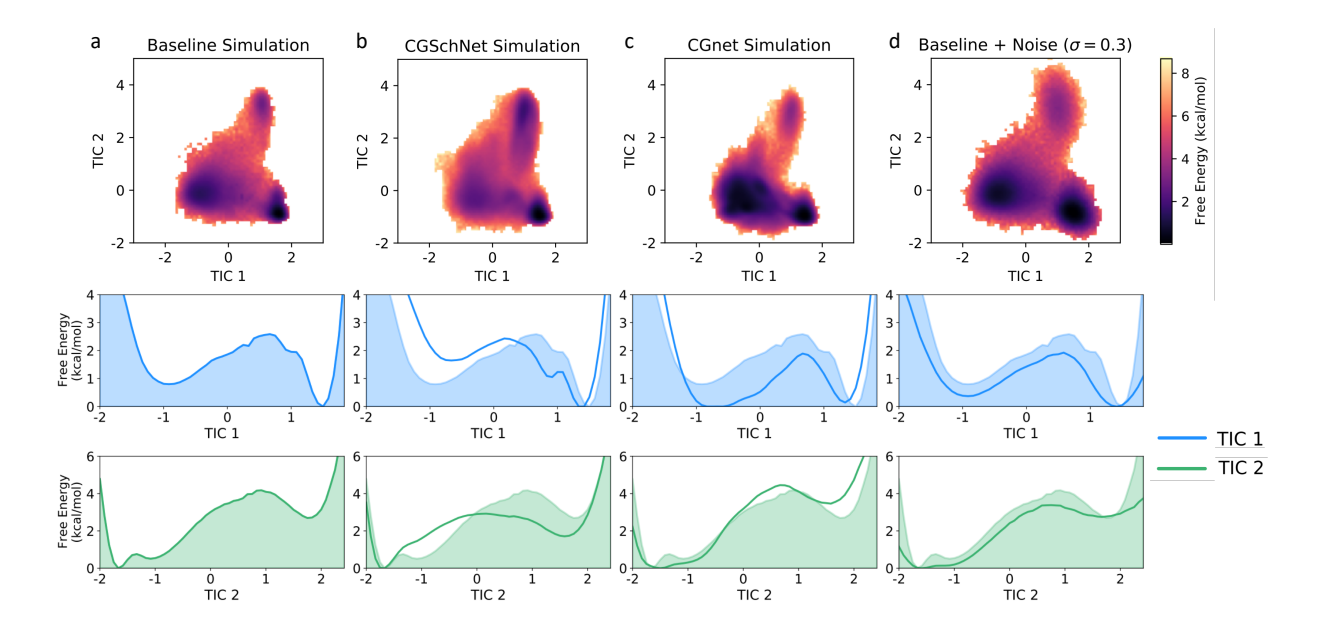


FIG. 7. Two- and one-dimensional free energy surfaces for five capped alanine datasets. From left to right, datasets are the baseline chignolin simulation (a), the coarse-grained CGSchNet simulation (b), the coarse-grained CGnet simulation (c), and the dataset generated from the perturbation of the original Cartesian coordinates of the baseline dataset drawn from noise distributed as $\sim \mathcal{N}(0,\sigma^2)$ for $\sigma=0.3$ Å (d). Each two-dimensional surface is obtained from a 120 × 120 histogram on TIC 1 × TIC 2 space with weights determined from the MSM built for each system (see main text). The one-dimensional surfaces are similarly obtained from 120-bin histograms on a single TIC. For each reweighted histogram bin, the free energy is obtained by taking the natural log of the counts and multiplying by $-k_BT$; the color scale is the same in all five two-dimensional surfaces and darker color represents lower free energy (i.e., greater stability). The shaded region always represents the baseline dataset and the bold line represents the dataset indicated in the subfigure title.

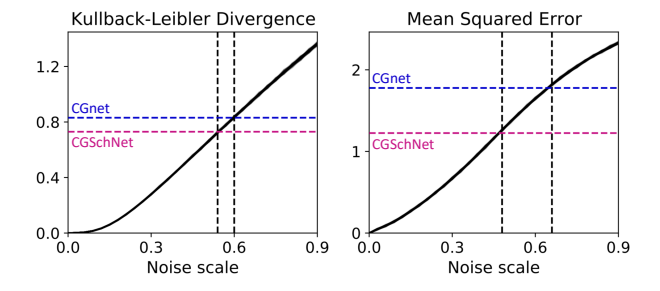


FIG. 8. The Kullback-Leibler divergence (left) and mean squared error (right) are calculated between the baseline dataset and the datasets obtained from perturbations to the baseline simulation at noise scale values of $\sigma \in$ $\{0, 0.03, 0.06, \dots, 0.90\}$ where the former is the reference distribution and the latter is the trial distribution. This procedure is performed 50 times with different random seeds; both plots show the superposition of those 50 lines. The colored horizontal dashed lines show the values of the metric when comparing the CGSchNet (purple) and the CGnet (blue) simulations to the baseline. The black vertical dashed line indicates the noise scale σ that return the closest value for that metric. The KL divergence is computed for normalized bin counts in reweighted TIC $1 \times TIC 2$ space, and the MSE is computed for energies as described in the main text.

used for the MSM analysis in this section are given in

Appendix E.

The stationary distribution of each MSM is then used to reweight the TICA coordinates used for its own construction. Histograms of the first two TICA coordinates are presented in the top row of Fig. 7 for the baseline, CGSchNet, and CGnet simulation datasets as well as the baseline dataset for $\sigma=0.3$. The first two reweighted TICA coordinates are also individually binned into one-dimensional free energy surfaces, which are depicted in the second and third rows of Fig. 7. We see that the free energy barriers along these reaction coordinates are reasonably approximated by the CGSchNet simulation.

Figure 8 shows the same divergence metrics calculated in Fig. 5 in the previous section. Again, we see that both the KL divergence and the MSE increase monotonically with the magnitude of the noise. In this case, we can assess the equivalent noise value for both the CGSchNet and CGnet simulation datasets. For both divergences measured, we see that the CGSchNet simulation corresponds to to a lesser value of added noise than the CGnet simulation.

We can also obtain free energy surfaces from the MSMs constructed for the systems; the surfaces for the baseline and CGSchNet simulation datasets of chignolin are presented in Fig. 9a on the left and right, respectively. We see that the three major basins observed in the atomistic data are captured by CGSchNet. These basins repre-

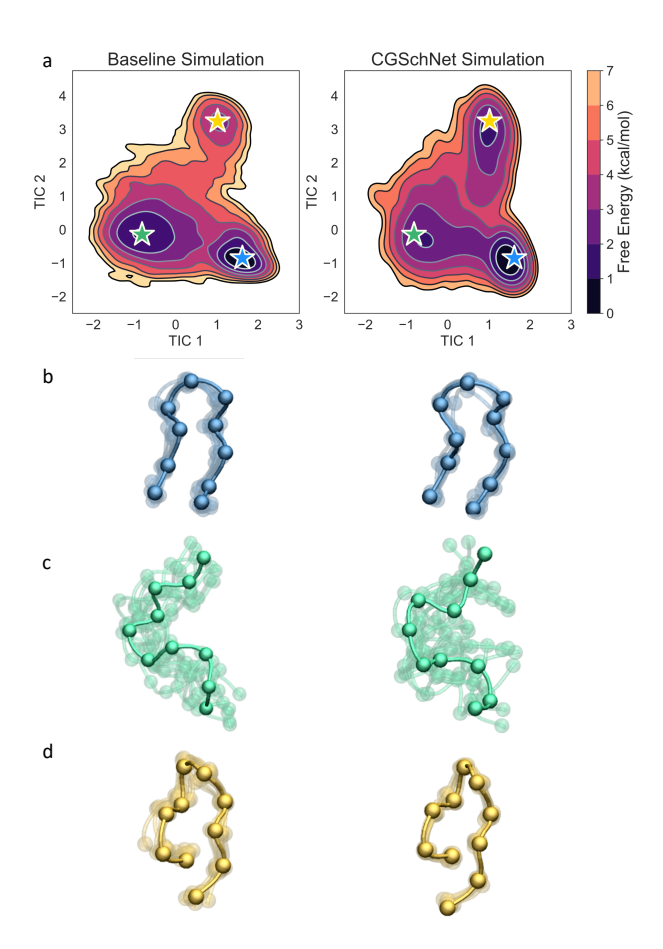


FIG. 9. Two-dimensional free energy surfaces (a) and sample folded (b), unfolded (c), and misfolded (d) conformations from the baseline atomistic simulation of chignolin (left column) and the CGSchNet simulation (right column). The free energy surfaces are built from 150-state MSMs that were constructed from the slowest two TICA coordinates in contact distance space. The color scale is the same for both surfaces and darker color represents lower free energy (i.e., greater stability). Each set of ten sampled structures corresponds to the MSM state represented by the star on the free energy surface of the same color (one of the ten structures opaque for clarity).

sent folded, unfolded, and misfolded ensembles and are indicated in Fig. 9a with blue, green, and yellow stars, respectively. Each star represents one of the 150 MSM states and was manually selected from the MSM states near the relevant basin (see Fig. A8 for a visualization of all 150 MSM states). To verify that the protein conformations are similar in each of the states, we sample ten structures from each starred state per simulation dataset. The structures are visualized in Fig. 9b-d, and the similarity of the structures on the left-hand side (baseline simulation) to those on the right-hand side (CGSchNet simulation) from corresponding MSM states is apparent.

The analysis of the CGSchNet and CGnet simulation datasets so far used TICA reaction coordinates that were obtained by projecting the simulation data onto coordinates defined by a TICA model built for the baseline

atomistic data (see Appendix E). This was done in order to compare simulation results using the same reaction coordinates. We can also construct TICA models from the simulation datasets without projection. For this analysis, we build two further (independent) TICA models for the CGSchNet and CGnet datasets. The first two timescales of the baseline TICA model lie above a spectral gap (see Fig. A7), and the absolute values of the Spearman rank correlation coefficients⁶⁹ between the corresponding TICA reaction coordinates from the baseline and CGSchNet TICA models are, respectively, 0.72 and 0.63 for the first and second TICA coordinates. This correlation analysis indicates that the corresponding slow processes capture the same collective motions. In contrast, the same correlations for the CGnet TICA model yield Spearman coefficients with absolute values of 0.68 and 0.24 for the first and second TICA coordinates, respectively.

Beyond noting that the slow collective motions captured by TICA are similar between the CGSchNet simulation and the atomistic simulation when no projection is used to model the former, we do not attempt a kinetic analysis in the present work because the scope of force matching is limited to thermodynamic consistency^{25,26}. The matching of dynamics in addition to thermodynamics is an open challenge that been the subject of recent work⁷⁰. Given coarse-grained dynamics, analytical methods have been derived that enable their rescaling to the dynamics of the system's all-atom counterpart⁷¹.

V. DISCUSSION

Coarse graining holds the promise of simulating larger systems at longer timescales than are currently possible at the atomistic level. However, mathematical frameworks must be developed in order to ensure that the results obtained from a coarse-grained model are faithful to those that would be obtained from an atomistic simulation or experimental measurement. Force matching ^{24,25} is one such framework that, when certain restrictions are applied, guarantees thermodynamic consistency with atomistic data in the variational limit ²⁶. Such a variational framework enables the formulation of the force matching problem as a supervised machine learning task, which is presented in Ref. 19 as CGnet.

A key limitation of the original CGnet is that it is not transferable: a new network must be trained for each individual molecular system under study because the molecular features from which it learns the force field must be chosen by hand. Here, we replace manually determined features with a learnable representation. This representation is enabled by the use of continuous filter convolutions on a graph neutral network (i.e., SchNet^{21,22}). SchNet is an inherently transferable architecture originally designed to match energies and forces to quantum calculations for small organic molecules. By leveraging SchNet in the *coarse graining* context—i.e., to learn the

molecular features input into a CGnet—we render the hybrid CGnet architecture (i.e., CGSchNet) fully transferable across molecular systems.

Our aim in the present contribution is threefold: to summarize the variational framework enabling a supervised learning approach to force matching, to provide an accompanying software package implementing the methods discussed herein (see Appendix F), and to demonstrate that CGSchNet produces results on individual systems that are superior to those obtained from bespoke features. The advances presented in this work prepare us to address the ultimate challenge of machine learning a coarse-grained force field that is transferable across molecular systems.

In our computational experiments performed on capped alanine and the miniprotein chignolin, we find that CGSchNet's performance exceeds that of CGnet in three ways. First, the free energy surface obtained from CGSchNet simulations of chignolin is more accurate than the free energy surface presented for the same systems in Ref. 19. Second, CGSchNet is more robust to network hyperparameters than its predecessor. In fact, for the CGSchNet hyperparameters varied during model training (see Appendix B), the same selections are used for both systems presented in Sec. IV. Third, CGSchNet employs less regularization; particularly, it does not require the extra step of enforcing a Lipschitz constraint⁵² on its network's weight matrices as was found to be necessary for CGnet¹⁹.

While our current protocol has demonstrated success for a capped monopeptide and a 10-amino acid miniprotein, adapting the CGSchNet pipeline to produce accurate coarse-grained force fields for larger protein systems remains an open challenge. Addressing this challenge may require specific sampling strategies when obtaining training data, the incorporation of new priors that inform tertiary structure formation, or modifications to the CGSchNet architecture itself such as regularization. Successfully modeling the thermodynamics of protein folding or conformational change via a transferable, machine-learned force field would signify a major success for the union of artificial intelligence and the computational molecular sciences.

Structural, bottom up coarse graining consists of two aspects: the model resolution and the force field. Here, we assume the resolution is set and focus on the force field, but the choice of an optimal model resolution is itself a significant challenge that is interconnected to the goal of force field optimization. How to choose a resolution for coarse graining—and the interplay of this choice with transferable force field architectures—remains an open question. Recent work has employed machine learning and data-driven approaches to pursue an optimal resolution using various objectives ^{15,16}.

Altogether, the methodology we introduce in the present contribution establishes a transferable architecture for the machine learning of coarse-grained force fields, and we expect our accompanying software to fa-

cilitate progress not only in that realm but also towards the outstanding challenges of learning coarse-grained dynamics and optimizing a model's resolution.

ACKNOWLEDGEMENTS

B.E.H. is immeasurably grateful to Moritz Hoffmann for his wisdom and support. The authors are grateful to Dr. Ankit Patel for discussions on model debugging and machine learning techniques, to Iryna Zaporozhets for discussions concerning model priors, and to Dr. Stefan Doerr for software help.

We acknowledge funding from the European Commission (ERC CoG 772230 "ScaleCell") to B.E.H., A.K, Y.C., and F.N; from MATH+ the Berlin Mathematics Center to B.E.H. (EF1-2), S.O. (AA1-6), and F.N (EF1-2 and AA1-6); from the Natural Science Foundation (CHE-1738990, CHE-1900374, and PHY-1427654) to N.E.C., J.W., and C.C.; from the Welch Foundation (C-1570) to N.E.C, J.W., and C.C.; from the NLM Training Program in Biomedical Informatics and Data Science (5T15LM007093-27) to N.E.C.; from the Einstein Foundation Berlin to C.C.; and from the Deutsche Forschungsgemeinschaft (SFB1114 projects A04 and C03) to F.N. D.L. was supported by a FPI fellowship from the Spanish Ministry of Science and Innovation (MICINN, PRE2018-085169). G.D.F. acknowledges support from MINECO (Unidad de Excelencia Mariá de Maeztu AEI [CEX2018-000782-M] and BIO2017-82628-P) and FEDER. This project has received funding from the European Union's Horizon 2020 research and innovation programme under Grant Agreement 823712 (CompBioMed2 Project). We thank the GPUGRID donors for their compute time.

Simulations were performed on the computer clusters of the Center for Research Computing at Rice University, supported in part by the Big-Data Private-Cloud Research Cyberinfrastructure MRI-award (NSF grant CNS-1338099), and on the clusters of the Department of Mathematics and Computer Science at Freie Universität, Berlin.

Part of this research was performed while B.E.H., N.E.C., D.L., J.W., G.dF., C.C., and F.N. were visiting the Institute for Pure and Applied Mathematics (IPAM) at the University of California, Los Angeles for the Long Program "Machine Learning for Physics and the Physics of Learning." IPAM is supported by the National Science Foundation (Grant No. DMS-1440415).

¹M. Shirts and V. S. Pande, "Screen savers of the world unite!" Science **290**, 1903–1904 (2000).

²F. Allen, G. Almasi, W. Andreoni, D. Beece, B. J. Berne, A. Bright, J. Brunheroto, C. Cascaval, J. Castanos, P. Coteus, P. Crumley, A. Curioni, M. Denneau, W. Donath, M. Eleftheriou, B. Flitch, B. Fleischer, C. J. Georgiou, R. Germain, M. Giampapa, D. Gresh, M. Gupta, R. Haring, H. Ho, P. Hochschild, S. Hummel, T. Jonas, D. Lieber, G. Martyna, K. Maturu, J. Moreira, D. Newns, M. Newton, R. Philhower, T. Picunko, J. Pitera, M. Pitman, R. Rand, A. Royyuru, V. Salapura,

A. Sanomiya, R. Shah, Y. Sham, S. Singh, M. Snir, F. Suits,

- R. Swetz, W. C. Swope, N. Vishnumurthy, T. J. C. Ward, H. Warren, and R. Zhou, "Blue gene: A vision for protein science using a petaflop supercomputer," IBM Syst. J. **40**, 310–327 (2001).
- ³I. Buch, M. J. Harvey, T. Giorgino, D. P. Anderson, and G. De Fabritiis, "High-throughput all-atom molecular dynamics simulations using distributed computing," J. Chem. Inf. Model. **50**, 397–403 (2010).
- ⁴D. E. Shaw, M. M. Deneroff, R. O. Dror, J. S. Kuskin, R. H. Larson, J. K. Salmon, C. Young, B. Batson, K. J. Bowers, J. C. Chao, M. P. Eastwood, J. Gagliardo, J. P. Grossman, C. R. Ho, D. J. Ierardi, I. Kolossváry, J. L. Klepeis, T. Layman, C. McLeavey, M. A. Moraes, R. Mueller, E. C. Priest, Y. Shan, J. Spengler, M. Theobald, B. Towles, and S. C. Wang, "Anton, a special-purpose machine for molecular dynamics simulation," Commun. ACM 51, 91–97 (2008).
- ⁵T. J. Lane, D. Shukla, K. A. Beauchamp, and V. S. Pande, "To milliseconds and beyond: challenges in the simulation of protein folding," Curr. Opin. Struct. Biol. **23**, 58–65 (2013).
- ⁶N. Plattner, S. Doerr, G. De Fabritiis, and F. Noé, "Complete protein-protein association kinetics in atomic detail revealed by molecular dynamics simulations and Markov modelling," Nat. Chem. 9, 1005 (2017).
- ⁷S. Kmiecik, D. Gront, M. Kolinski, L. Wieteska, A. E. Dawid, and A. Kolinski, "Coarse-grained protein models and their applications," Chem. Rev. 116, 7898–7936 (2016).
- ⁸C. Clementi, H. Nymeyer, and J. N. Onuchic, "Topological and energetic factors: what determines the structural details of the transition state ensemble and "en-route" intermediates for protein folding? an investigation for small globular proteins," J. Mol. Biol. 298, 937–953 (2000).
- ⁹S. J. Marrink, H. J. Risselada, S. Yefimov, D. P. Tieleman, and A. H. De Vries, "The MARTINI force field: coarse grained model for biomolecular simulations," J. Phys. Chem. B 111, 7812–7824 (2007).
- ¹⁰L. Monticelli, S. K. Kandasamy, X. Periole, R. G. Larson, D. P. Tieleman, and S.-J. Marrink, "The MARTINI coarse-grained force field: extension to proteins," J. Chem. Theory Comput. 4, 819–834 (2008).
- ¹¹A. Koliński *et al.*, "Protein modeling and structure prediction with a reduced representation," Acta Biochimica Polonica **51**, 349–371 (2004).
- ¹²A. Davtyan, N. P. Schafer, W. Zheng, C. Clementi, P. G. Wolynes, and G. A. Papoian, "AWSEM-MD: protein structure prediction using coarse-grained physical potentials and bioinformatically based local structure biasing," J. Phys. Chem. B 116, 8494–8503 (2012).
- ¹³R. Das and D. Baker, "Macromolecular modeling with Rosetta," Annu. Rev. Biochem. **77**, 363–382 (2008).
- ¹⁴W. G. Noid, "Perspective: Coarse-grained models for biomolecular systems," J. Chem. Phys. **139**, 090901 (2013).
- ¹⁵L. Boninsegna, R. Banisch, and C. Clementi, "A data-driven perspective on the hierarchical assembly of molecular structures," J. Chem. Theory Comput. 14, 453–460 (2018).
- ¹⁶W. Wang and R. Gómez-Bombarelli, "Coarse-graining autoencoders for molecular dynamics," npj Comput. Mater. 5, 1–9 (2019).
- ¹⁷S. John and G. Csányi, "Many-body coarse-grained interactions using gaussian approximation potentials," J. Phys. Chem. B 121, 10934–10949 (2017).
- ¹⁸L. Zhang, J. Han, H. Wang, R. Car, and W. E, "DeePCG: Constructing coarse-grained models via deep neural networks," J. Chem. Phys. **149**, 034101 (2018).
- ¹⁹J. Wang, S. Olsson, C. Wehmeyer, A. Pérez, N. E. Charron, G. De Fabritiis, F. Noé, and C. Clementi, "Machine learning of coarse-grained molecular dynamics force fields," ACS Cent. Sci. 5, 755–767 (2019).
- ²⁰ J. Wang, S. Chmiela, K.-R. Müller, F. Noé, and C. Clementi, "Ensemble learning of coarse-grained molecular dynamics force fields with a kernel approach," J. Chem. Phys. **152**, 194106

- (2020).
- ²¹K. Schütt, P.-J. Kindermans, H. E. Sauceda Felix, S. Chmiela, A. Tkatchenko, and K.-R. Müller, "SchNet: A continuous-filter convolutional neural network for modeling quantum interactions," in *Advances in Neural Information Processing Systems* 30, edited by I. Guyon, U. V. Luxburg, S. Bengio, H. Wallach, R. Fergus, S. Vishwanathan, and R. Garnett (Curran Associates, Inc., 2017) pp. 991–1001.
- ²²K. T. Schütt, H. E. Sauceda, P.-J. Kindermans, A. Tkatchenko, and K.-R. Müller, "SchNet-a deep learning architecture for molecules and materials," J. Chem. Phys. 148, 241722 (2018).
- ²³S. Honda, T. Akiba, Y. S. Kato, Y. Sawada, M. Sekijima, M. Ishimura, A. Ooishi, H. Watanabe, T. Odahara, and K. Harata, "Crystal structure of a ten-amino acid protein," J. Am. Chem. Soc. **130**, 15327–15331 (2008).
- ²⁴F. Ercolessi and J. B. Adams, "Interatomic potentials from first-principles calculations: the force-matching method," Europhys. Lett. 26, 583 (1994).
- ²⁵S. Izvekov and G. A. Voth, "A multiscale coarse-graining method for biomolecular systems," J. Phys. Chem. B **109**, 2469–2473 (2005).
- ²⁶W. G. Noid, J.-W. Chu, G. S. Ayton, V. Krishna, S. Izvekov, G. A. Voth, A. Das, and H. C. Andersen, "The multiscale coarse-graining method. I. A rigorous bridge between atomistic and coarse-grained models," J. Chem. Phys. 128, 244114 (2008).
- ²⁷S. Izvekov, M. Parrinello, C. J. Burnham, and G. A. Voth, "Effective force fields for condensed phase systems from ab initio molecular dynamics simulation: A new method for forcematching," J. Chem. Phys. 120, 10896–10913 (2004).
- ²⁸M. Guenza, M. Dinpajooh, J. McCarty, and I. Lyubimov, "Accuracy, transferability, and efficiency of coarse-grained models of molecular liquids," J. Phys. Chem. B **122**, 10257–10278 (2018).
- ²⁹S. Izvekov and G. A. Voth, "Multiscale coarse graining of liquidstate systems," J. Chem. Phys. **123**, 134105 (2005).
- ³⁰G. Ciccotti, T. Lelievre, and E. Vanden-Eijnden, "Projection of diffusions on submanifolds: Application to mean force computation," Comm. Pure Appl. Math. 61, 371–408 (2008).
- ³¹M. S. Shell, "The relative entropy is fundamental to multiscale and inverse thermodynamic problems," J. Chem. Phys. **129**, 144108 (2008).
- ³²J. F. Rudzinski and W. G. Noid, "Coarse-graining entropy, forces, and structures," J. Chem. Phys. **135**, 214101 (2011).
- ³³W. G. Noid, P. Liu, Y. Wang, J.-W. Chu, G. S. Ayton, S. Izvekov, H. C. Andersen, and G. A. Voth, "The multiscale coarse-graining method. II. Numerical implementation for coarse-grained molecular models," J. Chem. Phys. **128**, 244115 (2008).
- ³⁴T. T. Foley, M. S. Shell, and W. G. Noid, "The impact of resolution upon entropy and information in coarse-grained models," J. Chem. Phys. **143**, 243104 (2015).
- ³⁵A. Paszke, S. Gross, F. Massa, A. Lerer, J. Bradbury, G. Chanan, T. Killeen, Z. Lin, N. Gimelshein, L. Antiga, A. Desmaison, A. Kopf, E. Yang, Z. DeVito, M. Raison, A. Tejani, S. Chilamkurthy, B. Steiner, L. Fang, J. Bai, and S. Chintala, "Pytorch: An imperative style, high-performance deep learning library," in Advances in Neural Information Processing Systems 32, edited by H. Wallach, H. Larochelle, A. Beygelzimer, F. dAlché Buc, E. Fox, and R. Garnett (Curran Associates, Inc., 2019) pp. 8024–8035.
- ³⁶J. Behler and M. Parrinello, "Generalized neural-network representation of high-dimensional potential-energy surfaces," Phys. Rev. Lett. 98, 146401 (2007).
- ³⁷A. P. Bartók, M. C. Payne, R. Kondor, and G. Csányi, "Gaussian approximation potentials: The accuracy of quantum mechanics, without the electrons," Phys. Rev. Lett. **104**, 136403 (2010).
- ³⁸M. Rupp, A. Tkatchenko, K.-R. Müller, and O. A. Von Lilienfeld, "Fast and accurate modeling of molecular atomization energies with machine learning," Phys. Rev. Lett. **108**, 058301 (2012).

- ³⁹A. P. Bartók, M. J. Gillan, F. R. Manby, and G. Csányi, "Machine-learning approach for one-and two-body corrections to density functional theory: Applications to molecular and condensed water," Phys. Rev. B 88, 054104 (2013).
- ⁴⁰J. S. Smith, O. Isayev, and A. E. Roitberg, "ANI-1: an extensible neural network potential with DFT accuracy at force field computational cost," Chem. Sci. 8, 3192–3203 (2017).
- ⁴¹S. Chmiela, A. Tkatchenko, H. E. Sauceda, I. Poltavsky, K. T. Schütt, and K.-R. Müller, "Machine learning of accurate energy-conserving molecular force fields," Sci. Adv. 3, e1603015 (2017).
- ⁴²A. P. Bartók, S. De, C. Poelking, N. Bernstein, J. R. Kermode, G. Csányi, and M. Ceriotti, "Machine learning unifies the modeling of materials and molecules," Sci. Adv. 3, e1701816 (2017).
- ⁴³K. T. Schütt, F. Arbabzadah, S. Chmiela, K. R. Müller, and A. Tkatchenko, "Quantum-chemical insights from deep tensor neural networks," Nat. Commun. 8, 1–8 (2017).
- ⁴⁴J. S. Smith, B. Nebgen, N. Lubbers, O. Isayev, and A. E. Roitberg, "Less is more: Sampling chemical space with active learning," J. Chem. Phys. **148**, 241733 (2018).
- ⁴⁵A. Grisafi, D. M. Wilkins, G. Csányi, and M. Ceriotti, "Symmetry-adapted machine learning for tensorial properties of atomistic systems," Phys. Rev. Lett. **120**, 036002 (2018).
- ⁴⁶G. Imbalzano, A. Anelli, D. Giofré, S. Klees, J. Behler, and M. Ceriotti, "Automatic selection of atomic fingerprints and reference configurations for machine-learning potentials," J. Chem. Phys. 148, 241730 (2018).
- ⁴⁷T. T. Nguyen, E. Székely, G. Imbalzano, J. Behler, G. Csányi, M. Ceriotti, A. W. Götz, and F. Paesani, "Comparison of permutationally invariant polynomials, neural networks, and gaussian approximation potentials in representing water interactions through many-body expansions," J. Chem. Phys. 148, 241725 (2018).
- ⁴⁸L. Zhang, J. Han, H. Wang, W. Saidi, R. Car, and W. E, "End-to-end symmetry preserving inter-atomic potential energy model for finite and extended systems," in *Advances in Neu-ral Information Processing Systems 31*, edited by S. Bengio, H. Wallach, H. Larochelle, K. Grauman, N. Cesa-Bianchi, and R. Garnett (Curran Associates, Inc., 2018) pp. 4436–4446.
- ⁴⁹L. Zhang, J. Han, H. Wang, R. Car, and E. Weinan, "Deep potential molecular dynamics: a scalable model with the accuracy of quantum mechanics," Phys. Rev. Lett. **120**, 143001 (2018).
- ⁵⁰T. Bereau, R. A. DiStasio Jr, A. Tkatchenko, and O. A. Von Lilienfeld, "Non-covalent interactions across organic and biological subsets of chemical space: Physics-based potentials parametrized from machine learning," J. Chem. Phys. 148, 241706 (2018).
- ⁵¹H. Wang and W. Yang, "Toward building protein force fields by residue-based systematic molecular fragmentation and neural network," J. Chem. Phys. 15, 1409–1417 (2018).
- ⁵²H. Gouk, E. Frank, B. Pfahringer, and M. Cree, "Regularisation of neural networks by enforcing Lipschitz continuity," arXiv preprint arXiv:1804.04368 (2018).
- ⁵³D. P. Kingma and J. Ba, "Adam: A method for stochastic optimization," arXiv preprint arXiv:1412.6980 (2014).
- ⁵⁴T. Schneider and E. Stoll, "Molecular-dynamics study of a threedimensional one-component model for distortive phase transitions," Phys. Rev. B **17**, 1302 (1978).
- ⁵⁵J. Fass, D. A. Sivak, G. E. Crooks, K. A. Beauchamp, B. Leimkuhler, and J. D. Chodera, "Quantifying configurationsampling error in langevin simulations of complex molecular systems," Entropy 20, 318 (2018).
- ⁵⁶J. Gilmer, S. S. Schoenholz, P. F. Riley, O. Vinyals, and G. E. Dahl, "Neural message passing for quantum chemistry," in Proceedings of the 34th International Conference on Machine Learning-Volume 70 (JMLR. org, 2017) pp. 1263–1272.
- ⁵⁷K. Schutt, P. Kessel, M. Gastegger, K. Nicoli, A. Tkatchenko, and K.-R. Müller, "SchNetPack: A deep learning toolbox for atomistic systems," J. Chem. Theory Comput. **15**, 448–455 (2018).
- ⁵⁸K. He, X. Zhang, S. Ren, and J. Sun, "Deep residual learning for

- image recognition," in Proceedings of the IEEE Conference on Computer Vision and Pattern Recognition (2016) pp. 770–778.
- ⁵⁹S. Kullback and R. A. Leibler, "On information and sufficiency," Ann. Math. Stat. **22**, 79–86 (1951).
- ⁶⁰K. Lindorff-Larsen, S. Piana, R. O. Dror, and D. E. Shaw, "How fast-folding proteins fold," Science 334, 517–520 (2011).
- ⁶¹K. A. Beauchamp, R. McGibbon, Y.-S. Lin, and V. S. Pande, "Simple few-state models reveal hidden complexity in protein folding," Proc. Natl. Acad. Sci. **109**, 17807–17813 (2012).
- ⁶²B. E. Husic, R. T. McGibbon, M. M. Sultan, and V. S. Pande, "Optimized parameter selection reveals trends in Markov state models for protein folding," J. Chem. Phys. **145**, 194103 (2016).
- ⁶³K. A. McKiernan, B. E. Husic, and V. S. Pande, "Modeling the mechanism of CLN025 beta-hairpin formation," J. Chem. Phys. 147, 104107 (2017).
- ⁶⁴M. M. Sultan and V. S. Pande, "Automated design of collective variables using supervised machine learning," J. Chem. Phys. 149, 094106 (2018).
- ⁶⁵M. K. Scherer, B. E. Husic, M. Hoffmann, F. Paul, H. Wu, and F. Noé, "Variational selection of features for molecular kinetics," J. Chem. Phys. **150**, 194108 (2019).
- ⁶⁶B. E. Husic and V. S. Pande, "Markov state models: From an art to a science," J. Am. Chem. Soc. 140, 2386–2396 (2018).
- ⁶⁷G. Pérez-Hernández, F. Paul, T. Giorgino, G. De Fabritiis, and F. Noé, "Identification of slow molecular order parameters for Markov model construction," J. Chem. Phys. **139**, 015102 (2013).
- ⁶⁸C. R. Schwantes and V. S. Pande, "Improvements in Markov state model construction reveal many non-native interactions in the folding of NTL9," J. Chem. Theory Comput. 9, 2000–2009 (2013).
- ⁶⁹C. Spearman, "The proof and measurement of association between two things," Am. J. Psychol. 15, 72–101 (1904).
- ⁷⁰F. Nüske, L. Boninsegna, and C. Clementi, "Coarse-graining molecular systems by spectral matching," J. Chem. Phys. **151**, 044116 (2019).
- ⁷¹I. Lyubimov and M. Guenza, "First-principle approach to rescale the dynamics of simulated coarse-grained macromolecular liquids," Phys. Rev. E 84, 031801 (2011).
- ⁷²K. Lindorff-Larsen, S. Piana, K. Palmo, P. Maragakis, J. L. Klepeis, R. O. Dror, and D. E. Shaw, "Improved side-chain torsion potentials for the Amber ff99SB protein force field," Proteins: Struct., Funct., Bioinf. **78**, 1950–1958 (2010).
- ⁷³W. L. Jorgensen, J. Chandrasekhar, J. D. Madura, R. W. Impey, and M. L. Klein, "Comparison of simple potential functions for simulating liquid water," J. Chem. Phys. **79**, 926–935 (1983).
- ⁷⁴M. J. Harvey, G. Giupponi, and G. D. Fabritiis, "ACEMD: accelerating biomolecular dynamics in the microsecond time scale," J. Chem. Theory Comput. 5, 1632–1639 (2009).
- ⁷⁵S. Piana, K. Lindorff-Larsen, and D. E. Shaw, "How robust are protein folding simulations with respect to force field parameterization?" Biophys. J. **100**, L47–L49 (2011).
- ⁷⁶A. D. MacKerell Jr, D. Bashford, M. Bellott, R. L. Dunbrack Jr, J. D. Evanseck, M. J. Field, S. Fischer, J. Gao, H. Guo, S. Ha, et al., "All-atom empirical potential for molecular modeling and dynamics studies of proteins," J. Phys. Chem. B 102, 3586–3616 (1998).
- ⁷⁷J. A. Hartigan, Clustering Algorithms (John Wiley & Sons, Inc., 1975).
- ⁷⁸ J.-H. Prinz, H. Wu, M. Sarich, B. Keller, M. Senne, M. Held, J. D. Chodera, C. Schütte, and F. Noé, "Markov models of molecular kinetics: Generation and validation," J. Chem. Phys. 134, 174105 (2011).
- ⁷⁹T. F. Gonzalez, "Clustering to minimize the maximum intercluster distance," Theor. Comput. Sci. 38, 293–306 (1985).
- ⁸⁰R. Zwanzig, "From classical dynamics to continuous time random walks," J. of Stat. Phys. 30, 255–262 (1983).
- ⁸¹C. Schütte, A. Fischer, W. Huisinga, and P. Deuflhard, "A direct approach to conformational dynamics based on hybrid monte carlo," J. Comput. Phys. **151**, 146–168 (1999).

- ⁸²N. Singhal, C. D. Snow, and V. S. Pande, "Using path sampling to build better Markovian state models: predicting the folding rate and mechanism of a tryptophan zipper beta hairpin," J. Chem. Phys. 121, 415–425 (2004).
- ⁸³W. C. Swope, J. W. Pitera, and F. Suits, "Describing protein folding kinetics by molecular dynamics simulations. 1. Theory," J. Phys. Chem. B **108**, 6571–6581 (2004).
- ⁸⁴N.-V. Buchete and G. Hummer, "Coarse master equations for peptide folding dynamics," J. Phys. Chem. B **112**, 6057–6069 (2008).
- ⁸⁵C. D. Meyer, Matrix Analysis and Applied Linear Algebra, Vol. 71 (Siam, 2000).
- ⁸⁶L. Molgedey and H. G. Schuster, "Separation of a mixture of independent signals using time delayed correlations," Phys. Rev. Lett. **72**, 3634 (1994).
- ⁸⁷Y. Naritomi and S. Fuchigami, "Slow dynamics in protein fluctuations revealed by time-structure based independent component analysis: the case of domain motions," J. Chem. Phys. **134**, 065101 (2011).
- ⁸⁸R. T. McGibbon, B. E. Husic, and V. S. Pande, "Identification of simple reaction coordinates from complex dynamics," J. Chem. Phys. **146**, 044109 (2017).
- ⁸⁹H. Wu, F. Nüske, F. Paul, S. Klus, P. Koltai, and F. Noé, "Variational koopman models: slow collective variables and molecular kinetics from short off-equilibrium simulations," J. Chem. Phys. 146, 154104 (2017).
- ⁹⁰D. Sculley, "Web-scale k-means clustering," in *Proceedings of the 19th International Conference on World Wide Web* (2010) pp. 1177–1178.
- ⁹¹B. E. Husic and V. S. Pande, "Note: MSM lag time cannot be used for variational model selection," J. Chem. Phys. **147**, 176101 (2017).
- ⁹²C. Schütte and M. Sarich, Metastability and Markov State Models in Molecular Dynamics, Vol. 24 (American Mathematical Soc., 2013).
- ⁹³G. R. Bowman, V. S. Pande, and F. Noé, An introduction to Markov state models and their application to long timescale molecular simulation, Vol. 797 (Springer Science & Business Media, 2013).
- ⁹⁴W. Wang, S. Cao, L. Zhu, and X. Huang, "Constructing Markov state models to elucidate the functional conformational changes of complex biomolecules," WIREs Comput. Mol. Sci. 8, e1343 (2018).
- ⁹⁵F. Noé and F. Nuske, "A variational approach to modeling slow processes in stochastic dynamical systems," Multiscale Model. Simul. 11, 635–655 (2013).
- ⁹⁶R. T. McGibbon and V. S. Pande, "Variational cross-validation of slow dynamical modes in molecular kinetics," J. Chem. Phys. 142, 124105 (2015).
- ⁹⁷M. K. Scherer, B. Trendelkamp-Schroer, F. Paul, G. Pérez-Hernández, M. Hoffmann, N. Plattner, C. Wehmeyer, J.-H. Prinz, and F. Noé, "PyEMMA 2: A software package for estimation, validation, and analysis of Markov models," J. Chem. Theory Comput. 11, 5525–5542 (2015).
- ⁹⁸C. Wehmeyer, M. K. Scherer, T. Hempel, B. E. Husic, S. Olsson, and F. Noé, "Introduction to Markov state modeling with the PyEMMA software—v1. 0," LiveCoMS 1, 1–12 (2018).
- ⁹⁹M. P. Harrigan, M. M. Sultan, C. X. Hernández, B. E. Husic, P. Eastman, C. R. Schwantes, K. A. Beauchamp, R. T. McGibbon, and V. S. Pande, "MSMBuilder: statistical models for biomolecular dynamics," Biophys. J. **112**, 10–15 (2017).
- ¹⁰⁰ J. Porter, M. I. Zimmerman, and G. R. Bowman, "Enspara: Modeling molecular ensembles with scalable data structures and parallel computing," J. Chem. Phys. **150**, 044108 (2019).
- ¹⁰¹S. Van Der Walt, S. C. Colbert, and G. Varoquaux, "The NumPy array: a structure for efficient numerical computation," Comput. Sci. Eng. 13, 22 (2011).
- ¹⁰²E. Jones, T. Oliphant, P. Peterson, et al., "SciPy: Open source scientific tools for Python," (2001–).
- $^{103}\mathrm{W}.$ McKinney et~al., "Data structures for statistical computing

- in python," in *Proceedings of the 9th Python in Science Conference*, Vol. 445 (Austin, TX, 2010) pp. 51–56.
- ¹⁰⁴R. T. McGibbon, K. A. Beauchamp, M. P. Harrigan, C. Klein, J. M. Swails, C. X. Hernández, C. R. Schwantes, L.-P. Wang, T. J. Lane, and V. S. Pande, "MDTraj: a modern open library for the analysis of molecular dynamics trajectories," Biophys. J. 109, 1528–1532 (2015).
- ¹⁰⁵F. Pedregosa, G. Varoquaux, A. Gramfort, V. Michel, B. Thirion, O. Grisel, M. Blondel, P. Prettenhofer, R. Weiss, V. Dubourg, J. Vanderplas, A. Passos, D. Cournapeau, M. Brucher, M. Perrot, and E. Duchesnay, "Scikit-learn: Machine learning in Python," J. Mach. Learn. Res. 12, 2825–2830 (2011).
- ¹⁰⁶T. Kluyver, B. Ragan-Kelley, F. Pérez, B. Granger, M. Bussonnier, J. Frederic, K. Kelley, J. Hamrick, J. Grout, S. Corlay, P. Ivanov, D. Avila, S. Abdalla, and C. Willing, "Jupyter notebooks a publishing format for reproducible computational workflows," in *Positioning and Power in Academic Publishing: Players, Agents and Agendas*, edited by F. Loizides and B. Schmidt (IOS Press, 2016) pp. 87–90.
- ¹⁰⁷J. D. Hunter, "Matplotlib: A 2D graphics environment," Comput. Sci. Eng. 9, 90–95 (2007).
- ¹⁰⁸P. Eastman, J. Swails, J. D. Chodera, R. T. McGibbon, Y. Zhao, K. A. Beauchamp, L.-P. Wang, A. C. Simmonett, M. P. Harrigan, C. D. Stern, et al., "OpenMM 7: Rapid development of high performance algorithms for molecular dynamics," PLoS Comput. Biol. 13, e1005659 (2017).
- ¹⁰⁹M. Waskom, O. Botvinnik, D. O'Kane, P. Hobson, S. Lukauskas, D. C. Gemperline, T. Augspurger, Y. Halchenko, J. B. Cole, J. Warmenhoven, J. de Ruiter, C. Pye, S. Hoyer, J. Vanderplas, S. Villalba, G. Kunter, E. Quintero, P. Bachant, M. Martin, K. Meyer, A. Miles, Y. Ram, T. Yarkoni, M. L. Williams, C. Evans, C. Fitzgerald, Brian, C. Fonnesbeck, A. Lee, and A. Qalieh, "mwaskom/seaborn: v0.8.1 (september 2017)," (2017).
- ¹¹⁰W. Humphrey, A. Dalke, and K. Schulten, "VMD Visual Molecular Dynamics," J. Mol. Graph. 14, 33–38 (1996).
- ¹¹¹B. Trendelkamp-Schroer, H. Wu, F. Paul, and F. Noé, "Estimation and uncertainty of reversible Markov models," J. Chem. Phys. **143**, 174101 (2015).

Appendix A: Baseline simulation datasets

A single capped alanine simulation was performed in explicit solvent (2, 269 total atoms) at a temperature of 300 K with the AMBER ff99SB-ILDN force field⁷² and the TIP3P water model⁷³. All bonds between hydrogens and heavy atoms were constrained. The dataset represents 1 μ s of simulation time with coordinates and forces saved at 1 ps intervals for a total of 10⁶ frames. This simulation took about 2 days on a GTX1080 GPU.

The miniprotein chignolin²³ was simulated on GPU grid³ with ACEMD⁷⁴ using an adaptive sampling scheme in which new trajectories were respawned from the least explored states. The explicit solvent system contained 5820 atoms and was simulated at a temperature of 350 K with the CHARMM22* force field⁷⁵ and the mTIP3P water model⁷⁶. The dataset comprises 180 μ s of simulation time with coordinates and forces saved at 100 ps intervals for a total of 1.8×10^6 frames. The simulation (including server-to-client sending and retrieval) took a few weeks and employed up to thousands of GPUs.

Appendix B: CGSchNet hyperparameters

A CGSchNet was constructed for each of the systems reported in Sec. IV. In Table AI we enumerate all of the hyperparameters for the coarse-grained mapping, the SchNet feature, the remaining CGnet architecture (recall Fig. 1), and other training specifications.

TABLE AI. Hyperparameter choices for CGSchNet models trained on capped alanine and chignolin systems. Parameters listed in brackets were optimized using cross-validation; the underlined number is the starting value and the bold number is the value determined through cross-validation.

determined through cross-vandation.			
Hyperparameter	Capped alanine	Chignolin (CGSchNet)	Chignolin (CGnet) ^a
Sequence	ACE-ALA-NME	YYDPETGTWY	YYDPETGTWY
Number of coarse-grained beads	6	10	10
CG atom types	$2 \times N, C_{\alpha}, C_{\beta}, 2 \times C$	$10 \times C_{\alpha}$	$10 \times C_{\alpha}$
Embeddings	Nuclear	Per residue ^b	_
Harmonic priors	Bonds and angles	Bonds and angles	Bonds and angles
Repulsion priors	_	Non-bonded pairs ^c	Non-bonded pairs ^d
SchNet feature size	[32, 64, 128 , 256]	[32, 64, 128 , 256]	_
Number of SchNet basis functions	50	300	_
SchNet basis function bounds	$0 ext{ to } 5 ext{ Å}$	$0 ext{ to } 30 ext{ Å}$	_
SchNet neighbor cutoff	∞	∞	_
SchNet normalization	None	Bead number	_
Number of SchNet interaction blocks	[1, 2, 3, 5]	[1, 2, 3, 5]	_
SchNet activation function	Tanh	Tanh	_
Standard scaling before terminal network	No	No	Yes
Number of terminal network layers	[1 , 2, 3, 4, 5]	[1 , 2, 3, 4, 5]	5
Terminal network layer width	SchNet feature size	SchNet feature size	250
Terminal network activation function	Tanh	Tanh	Tanh
L_2 Lipschitz regularization ⁵²	_	_	4.0
Batch size	512	512	512
Number of epochs	100	100	20
Initial learning rate	6×10^{-4}	10^{-4}	3×10^{-3}
Learning rate scheduler ^e	Reduce on plateau ^f	None	Multi-step decay ^g
Optimizer	ADAM	ADAM	ADAM
Training/test set split	80%/20%	80%/20%	80%/20%
Cross-validation split strategy	Random	Random	Random
Number of cross-validation folds	5	5	5

The hyperparameters optimized under cross-validation were the number of interaction blocks and feature size in the internal SchNet, and the number of layers in the "terminal" CGnet network. The hyperparameters were varied in the order listed while holding the others constant; at each stage, a "final" hyperparameter was selected before the next one was varied. For each hyperparameter set, five models were trained according to the settings in Table AI, and the lowest test set loss of any (i.e., not necessarily the last) epoch was recorded. These losses are shown in Fig. A1.

The initial model explored for each system had five interaction blocks, a SchNet feature size of 128, and one layer in the terminal neural network. The first search was performed over interaction blocks; the left column of Fig. A1 shows that the average minimum loss was achieved with two interaction blocks for each system. The number of interaction blocks was then set to two, and the SchNet feature size was varied. A SchNet feature size of 128 was chosen for both systems both due to the value of the mean minimum losses and due to the relatively low variance of the test set loss values across the five folds (observed for both systems; see the middle column of Fig. A1). Finally, the number of layers in the terminal network was explored for two interaction blocks and a SchNet feature size of 128. The right column of Fig. A1 shows that increasing the number of terminal layers did not noticeably decrease the test set loss values for either system, and in some cases increased the variance across the five cross-validation runs. Thus for both systems we used a single layer for the terminal network component of the CGnet.

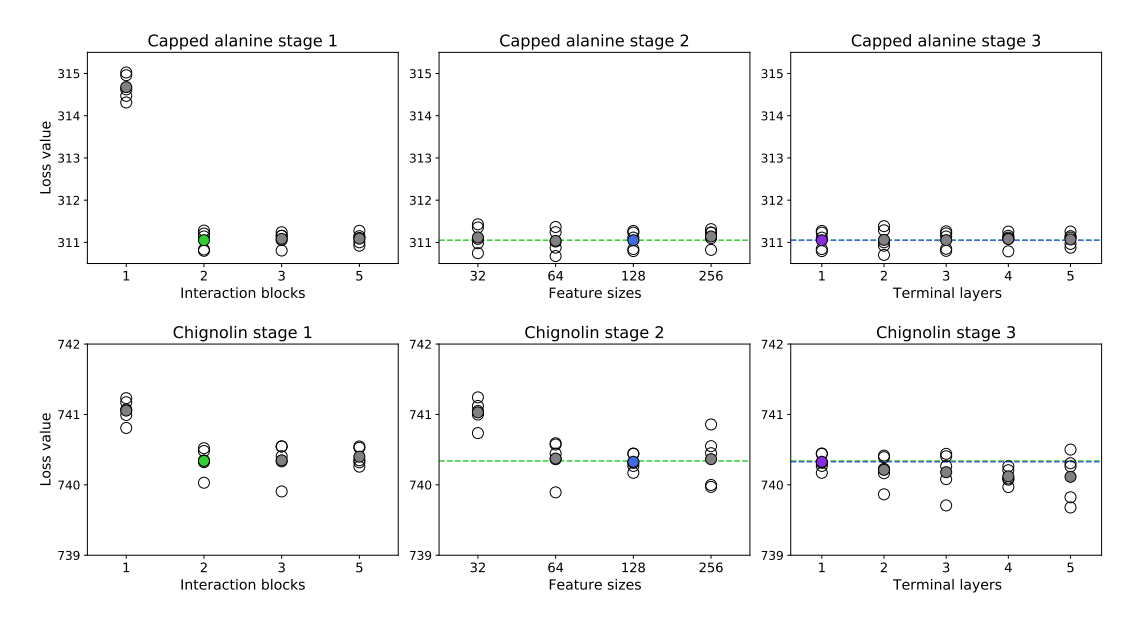


FIG. A1. Hyperparameter searches for capped alanine (top) and chignolin (bottom) for interaction blocks (left), SchNet feature sizes (center), and terminal network layers (right). The unfilled circles represent the minimum loss value obtained for that cross-validation run on the test dataset. The filled circle represents the average across the five runs. The filled circle is colored if that hyperparameter value was chosen for the "final" model. The dashed line shows the value of the average loss from the previous parameter search for the selected value of the previously explored parameter.

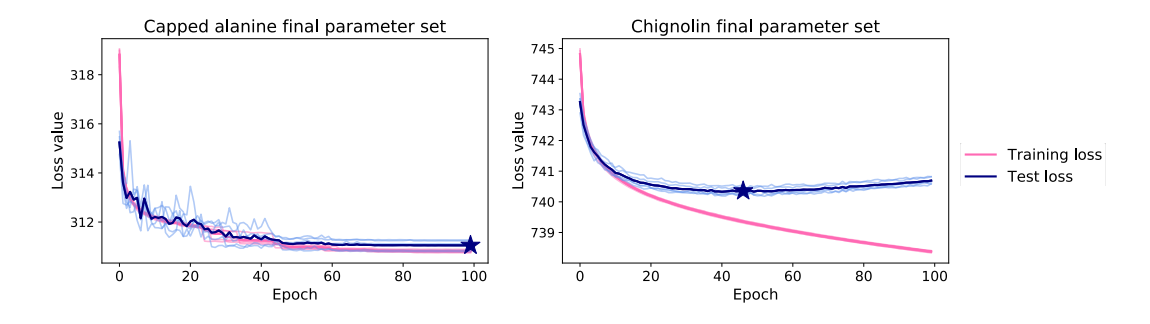


FIG. A2. Loss curves for the final parameter sets of CGSchNet models for capped alanine (left) and chignolin (right). Pink curves represent loss values on the training dataset and blue curves represent loss values on the test dataset. Each light-colored curve signifies one of the five runs and the dark-colored curve signifies the mean at each epoch. The training losses are so similar that the five distinct lines are not discernible. We chose which model to use for analysis and production according to the minimum of the test loss curve, which is indicated by the blue star (epoch 100 for capped alanine, epoch 46 for chignolin).

Appendix C: CGSchNet simulation details

After training CGSchNets and selecting hyperparameters as described in Sec. B, simulations in the coarse-grained space were performed for each system using Langevin dynamics (recall Sec. III A 7). These simulations represent an averaging of the five cross-validated folds of each final model: for each set of coarse-grained coordinates to be propagated forward by the time step, each of the five models predicts a set of forces, and those forces are averaged in their respective dimensions. It is this averaged force vector that the simulation integrator uses to propagate the coarse-grained coordinates in time. The parameters are listed in Table AII. The starting coordinates for the capped alanine CGSchNet simulation are shown on the right side of Fig. A3. Two trajectories that feature transitions among the major basins are visualized in Fig. A4; the same trajectories were used in Fig. 3.

TABLE AII. Parameters used for Langevin dynamics simulations of coarse-grained systems using a trained CGSchNet model.

Parameter	Capped alanine	Chignolin (CGSchNet)	Chignolin (CGnet)
Number of models averaged	5	5	5
Number of coarse-grained beads	6	10	10
Temperature (K)	300	350	350
Friction (ps^{-1})	490	490	490
Timestep (ps)	0.02	0.02	0.02
Number of independent simulations	100	100	100
Starting position selection algorithm	Regular spatial ^{77,78,a}	k-centers ⁷⁹	k-centers
Space for starting position selection	$\phi imes \psi$	$\mathrm{TIC}~1 imes \mathrm{TIC}~2^{\mathrm{b}}$	TIC $1 \times$ TIC 2
Number of timesteps	10^{6}	10^{6}	10^{6}
Output simulation stride (ps)	0.2	0.2	0.2
Total dataset time (μs)	20	20	20
Wall clock time to complete simulations (hours)	$24^{\rm c}$	14	13
Hardware	Tesla K80	GeForce GTX 1080	GeForce GTX 1080

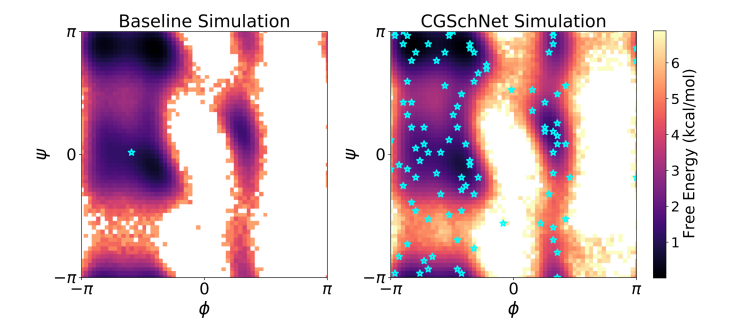


FIG. A3. Starting positions in Ramachandran space (blue stars) for the baseline (left) and CGSchNet simulations (right) of capped alanine. The free energy surfaces are reproduced from Fig. 4a and b, respectively.

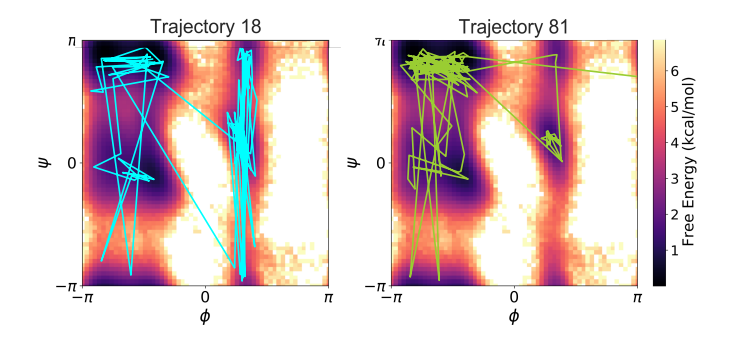


FIG. A4. Two individual CGSchNet simulation trajectories for capped alanine. Both trajectories sample the four major basins on the landscape. The free energy surfaces are both reproduced from Fig. 4b.

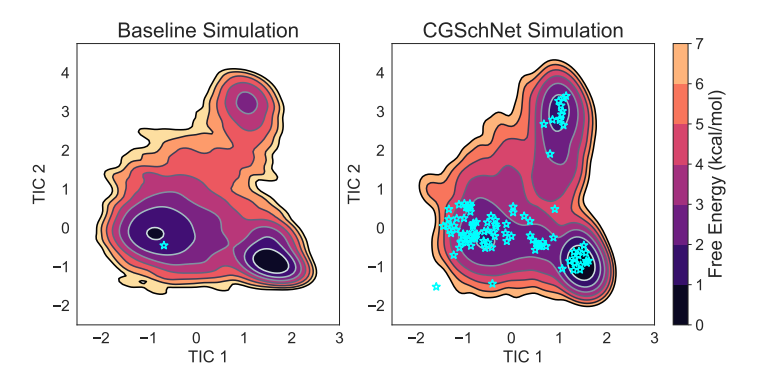


FIG. A5. Starting positions in TIC 1 \times TIC 2 space (blue stars) for the baseline (left) and CGSchNet simulations of chignolin (right). The free energy surfaces are reproduced from Fig. 9a.

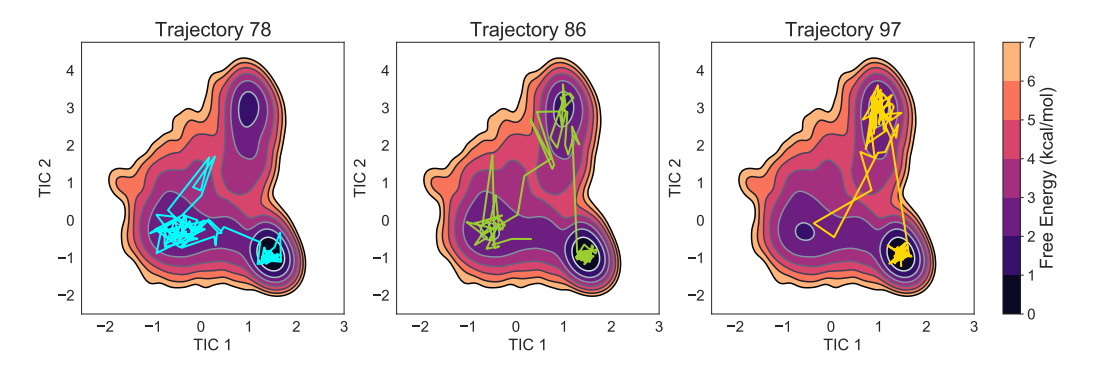


FIG. A6. Three individual CGSchNet simulation trajectories for chignolin. Each visualized simulation accesses multiple major basins. The free energy surfaces are reproduced from Fig. 9a.

Appendix D: Brief introduction to MSMs

Briefly, MSMs leverage the idea that mathematically straightforward kinetics emerge from a decomposition of simulation data into a set of states among which the transitions at a certain "lag time" τ are Markovian (i.e., dependent on only the present state of the system and independent of previous state occupations)^{80–84}. An MSM containing a set of discrete states is represented by a transition matrix $\mathbf{T}(\tau)$ that is row-stochastic, irreducible, and aperiodic (the latter two together are often referred to as "ergodic" in this context; this means every state can be reached from any other state without requiring cycles).

An MSM is typically constructed under the assumption that the Markov process is reversible with respect to its stationary distribution; this means it obeys the detailed balance constraint,

$$\pi(a)\Pr(a \to b) = \pi(b)\Pr(b \to a),$$
 (A1)

where, e.g., $\pi(a)$ is the stationary probability of being in state a and $\Pr(a \to b)$ is the probability of transitioning from state a to state b after a predetermined lag time. The equality of the left-hand and right-hand sides of (A1) means the system is microscopically reversible; i.e., at thermodynamic equilibrium.

This entails that the eigendecomposition of the MSM,

$$\mathbf{T}(\tau)\psi_i = \psi_i \lambda_i,\tag{A2}$$

has certain properties (according to the Perron-Frobenius theorem⁸⁵), namely, (i) the eigenvectors ψ_i and eigenvalues λ_i are real; particularly, (ii) the dominant (Perron) eigenvalue $\lambda_1 = 1$ and is unique, and its corresponding eigenvector ψ_1 has only positive elements which correspond to the stationary distribution π_i ; and (iii) the remaining eigenvalues $\lambda_i, i \geq 2$ have magnitudes less than 1 and their corresponding eigenvectors $\psi_i, i \geq 2$ have all real elements where negative and positive elements represent the fluxes out of and into MSM states, respectively. Using the lag time τ , the eigenvalues can be related to the timescales of the kinetic processes in the (equilibrium) system according to,

$$t_i \equiv \frac{-\tau}{\log|\lambda_i|}. (A3)$$

In practice, to construct an MSM we often use the following series of steps starting from the "raw" Cartesian coordinates of the simulation to be analyzed⁶²:

- 1. Featurization. The Cartesian coordinates output from the MD simulation are converted into a more useful representation according to properties known to be preserved in the system and/or chemical intuition. For example, the dynamics of proteins in a system without an external gradient are expected to be invariant to translation and rotation, so featurization schemes preserving these invariances are often employed. In proteins, two common featurizations are the backbone dihedral angles (cf. Sec. IV A) and distances between the amino acids (cf. Sec. IV B).
- 2. Dimensionality reduction. Optionally, a basis set transformation can be performed on the features to convert the data into a space in which the Markovian assumption is better satisfied. In the MSM community, time-lagged independent component analysis (TICA)^{67,68,86,87} is frequently used. TICA requires the calculation of two matrices,

$$\mathbf{C}_{\tau} \equiv \frac{\mathbf{X}^{\top} \mathbf{Y} + \mathbf{Y}^{\top} \mathbf{X}}{2(T - \tau)},\tag{A4a}$$

$$\mathbf{C}_0 \equiv \frac{\mathbf{X}^\top \mathbf{X} + \mathbf{Y}^\top \mathbf{Y}}{2(T - \tau)},\tag{A4b}$$

where $\mathbf{X} \in \mathbb{R}^{(T-\tau)\times n}$ is the time series data and $\mathbf{Y} \in \mathbb{R}^{(T-\tau)\times n}$ is the data shifted forward in time by an interval of τ for T total simulation time. Since (A4a) and (A4b) are both symmetric, the following generalized eigenvalue problem can be written,

$$\mathbf{C}_{\tau}\phi_{i} = \mathbf{C}_{0}\phi_{i}\lambda_{i},\tag{A5}$$

where the eigenvectors ϕ_i enable the transformation of the input data into TICA space. The TICA timescales can also be computed according to (A3). The TICA coordinates can be interpreted as reaction coordinates⁸⁸ and TICA may be used as a model in its own right⁶⁷ or as a step in the process of the construction of another kinetic model such as an MSM⁶⁸. Note that this harsh symmetry implementation may introduce significant bias⁸⁹.

- 3. State decomposition. In this step, the MSM states are assigned. A clustering algorithm such as k-means⁹⁰ is used to assign each data point in the MD simulation dataset to a discrete state. This means the simulation dataset is represented by a list of integers indicating the state to which each conformation belongs.
- 4. MSM estimation. Finally, the MSM is estimated from the cluster assignments. A Markovian lag time is designated⁹¹ and transitions are counted and stored in a "counts matrix." This counts matrix is converted to the MSM transition matrix $\mathbf{T}(\tau)$ using a maximum-likelihood estimation algorithm⁷⁸ such that it adheres to the previously described requirements of detailed balance and ergodicity.

A great deal of research has gone into MSM theory and practice which is summarized in books^{92,93} and recent reviews^{66,94}. A crucial advance that we do not go into here is the derivation of a variational principle for MSM construction that enables the optimization of the hyperparameters associated with the choices in items 1 through 3 when describing the system kinetics^{95,96}. Open source software packages facilitating MSM analyses include PyEMMA^{97,98}, MSMBuilder⁹⁹, and Enspara¹⁰⁰.

Appendix E: MSM construction for chignolin

To facilitate the majority of the analysis in Sec. IV B, MSMs (see Sec. D) were constructed for both the baseline atomistic dataset and the coarse-grained simulation datasets obtained from CGSchNet and CGnet.

To build an MSM for the atomistic MD dataset of chignolin, we first featurize the Cartesian coordinates into vectors of contact distances among every pair of amino acid residues. This transformation produces 45 distances, where the distances are defined as the distance between the two α -carbons. TICA is performed on the set of distances with a lag time of 10 ns. The eigenvalue spectrum of the baseline TICA model is presented in Fig. A7. We retained the first four TICA coordinates and used k-means to cluster the data in this four-dimensional space with k = 150. From the state space of 150 clusters, an MSM is estimated with a lag time of 15 ns.

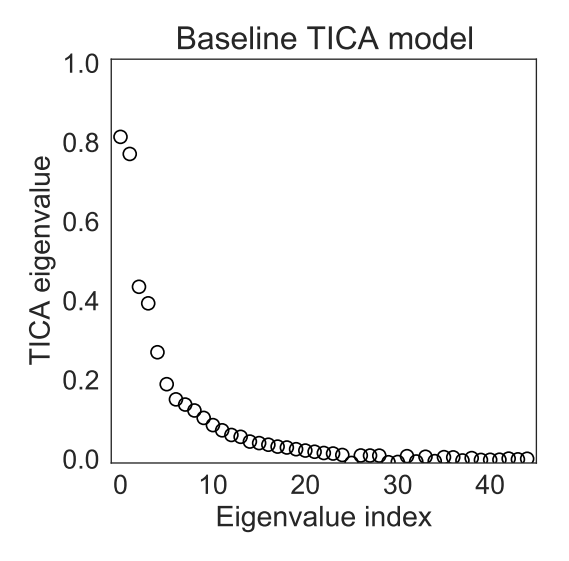


FIG. A7. Eigenvalue plot for the TICA model built upon the baseline atomistic simulation data.

For the CGSchNet simulation, we create a "projected" MSM which utilizes the TICA and clustering models built for the baseline MSM as previously described. This entails that the TICA and clustering spaces will be the same for both datasets, so the MSMs can be compared. We perform the same contact featurization on the coarse-grained simulation data. Instead of calculating a new TICA model, we project the featurized CGSchNet simulation data onto the TICs defined by the baseline TICA model. Similarly, we then assign each coarse-grained data point in TIC space

to one of the 150 clusters previously defined by the k-means model on the simulation data. An independent MSM is fit from these cluster assignments. The locations of the cluster centers are shown in Fig. A8.

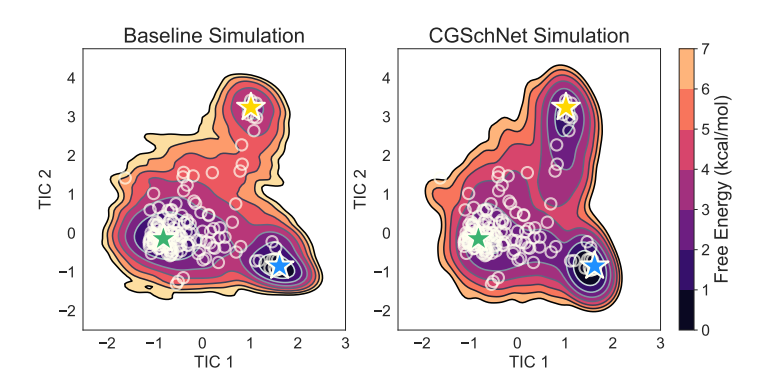


FIG. A8. Locations of 150 k-means cluster centers in TIC 1 × TIC 2 space (white circles) for the baseline (left) and CGSchNet simulations of chignolin (right). The cluster centers are identical in both plots. The free energy surfaces and starred MSM states are reproduced from Fig. 9a.

The lag time and k parameters were chosen based on the knowledge that chignolin has relatively simple kinetics 60,61 paired with the authors' familiarity with MSM construction for this specific system 19 and their experience that the modeled kinetics of chignolin are relatively robust to MSM hyperparameter choices 63 . In general it is crucial to use the variational method to determine MSM hyperparameters 95,96 . To validate our MSMs, we performed implied timescale 83 and Chapman-Kolmogorov 78 tests, which are shown on the following pages. The MSM lag time of 30 ns was chosen based on the implied timescale plots.

Appendix F: Software

The cgnet software package is available at https://github.com/coarse-graining/cgnet under the BSD-3-Clause license. cgnet requires NumPy¹⁰¹, SciPy¹⁰², and PyTorch³⁵, and optional functionalities further depend on pandas¹⁰³, MDTraj¹⁰⁴, and Scikit-learn¹⁰⁵. The examples are provided in Jupyter notebooks¹⁰⁶ which also require Matplotlib¹⁰⁷. The SchNet part of the code is inspired by SchNetPack⁵⁷ and the Langevin dynamics simulation code is adapted from OpenMM¹⁰⁸. In addition to cgnet and the packages already mentioned, visualization was aided by Seaborn¹⁰⁹ and VMD¹¹⁰. Analysis was facilitated by PyEMMA^{97,98}.

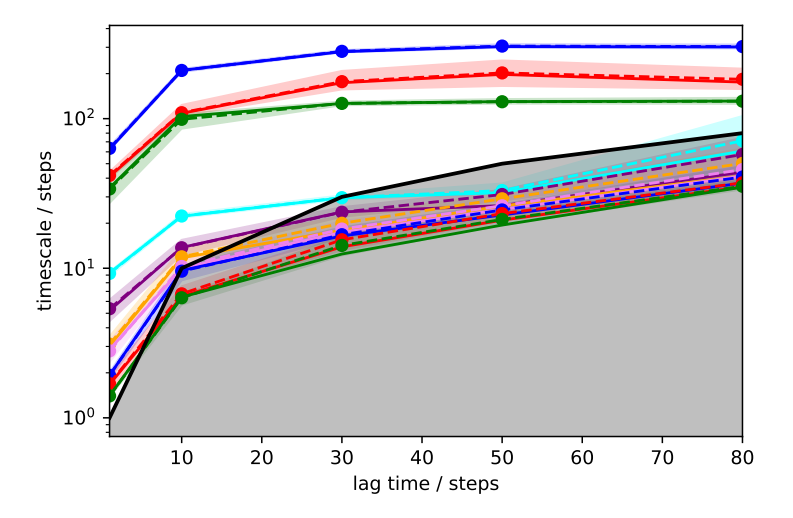


FIG. A9. Implied timescales test for a reversible Bayesian MSM^{111} constructed constructed from the baseline all-atom data for chignolin. The dashed line indicates the mean timescales, the solid line indicates the timescales of the maximum likelihood estimate, and the shaded region indicates a 95% confidence interval. A lag time of 30 frames was chosen.

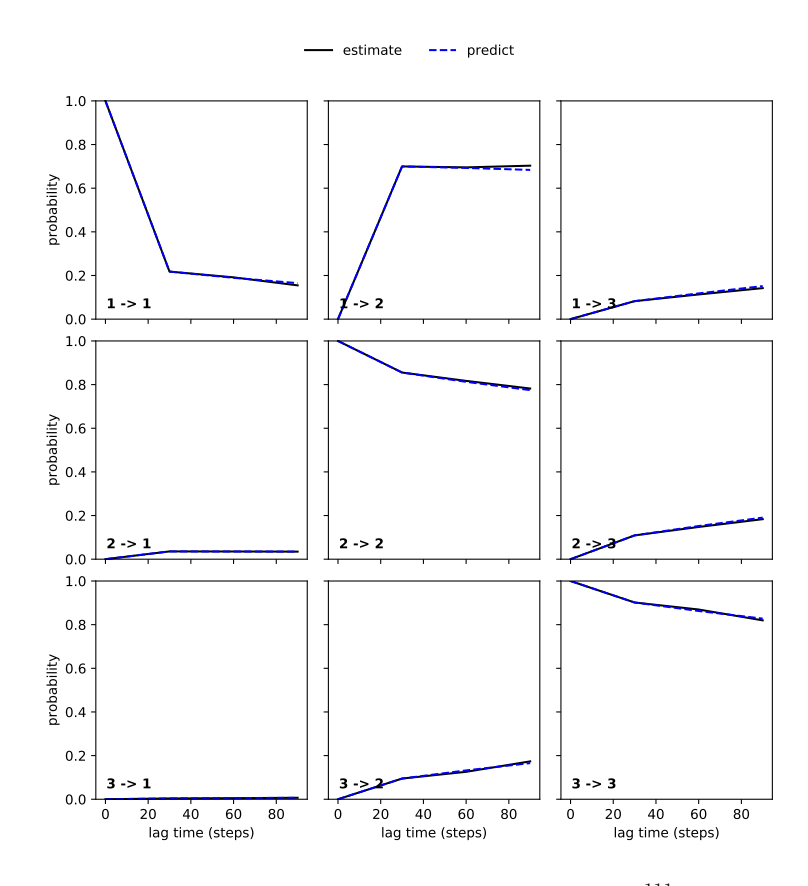


FIG. A10. Chapman-Kolmogorov test (3 macrostates) for a reversible Bayesian MSM^{111} constructed from the baseline all-atom data for chignolin. The dashed blue line is the prediction and black is the estimate.

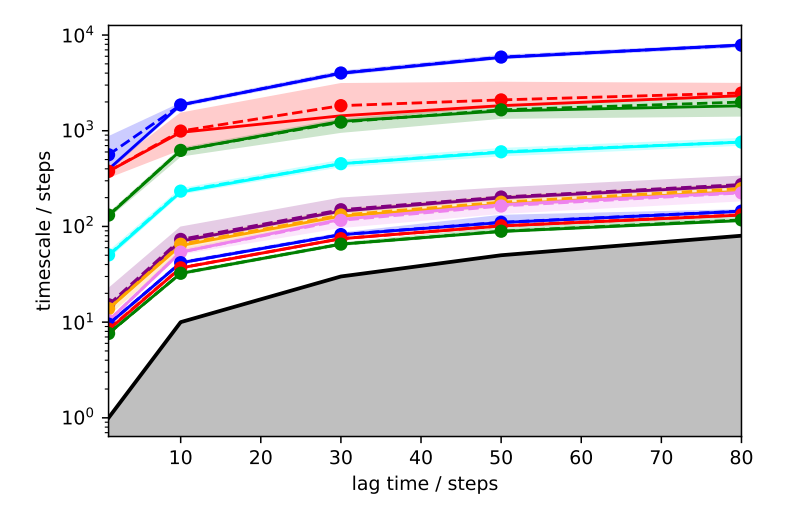


FIG. A11. Implied timescales test for a reversible Bayesian MSM^{111} constructed from the CGSchNet simulation data for chignolin. The dashed line indicates the mean timescales, the solid line indicates the timescales of the maximum likelihood estimate, and the shaded region indicates a 95% confidence interval. A lag time of 30 frames was chosen.

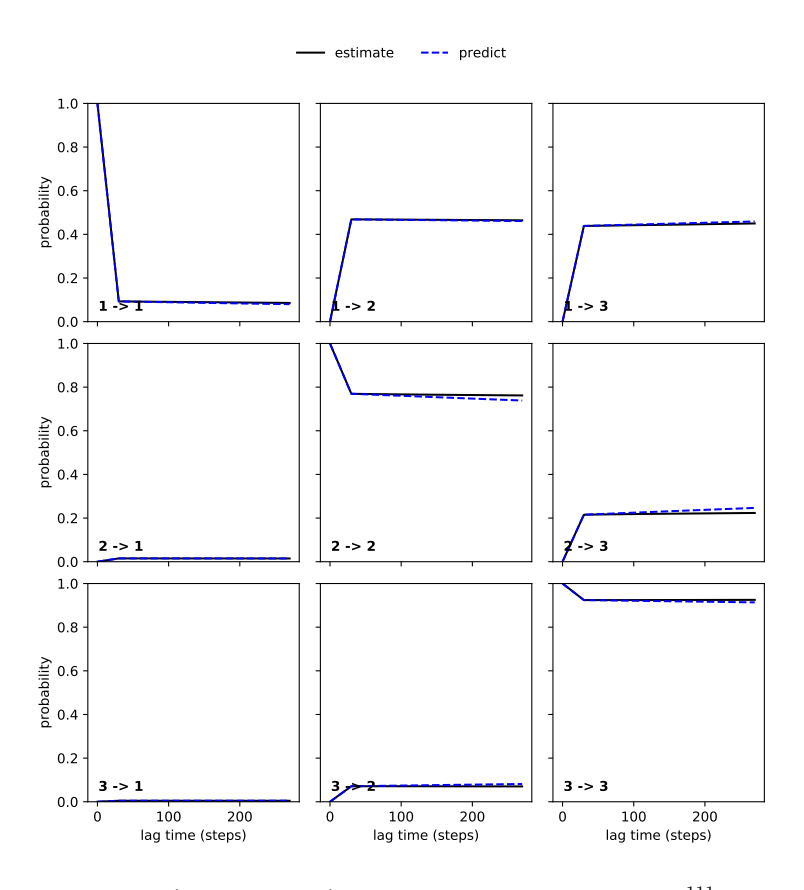


FIG. A12. Chapman-Kolmogorov test (3 macrostates) for a reversible Bayesian MSM¹¹¹ constructed from the CGSchNet simulation data for chignolin. The dashed blue line is the prediction and black is the estimate.

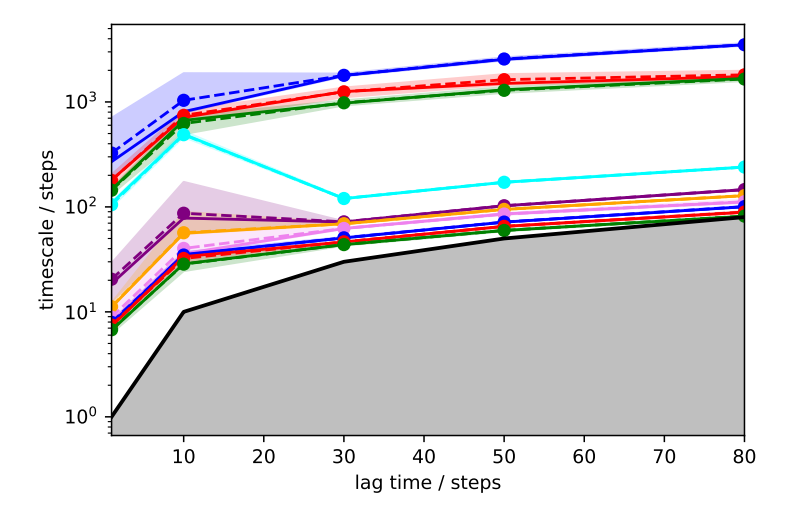


FIG. A13. Implied timescales test for a reversible Bayesian MSM^{111} constructed from the CGnet simulation data for chignolin. The dashed line indicates the mean timescales, the solid line indicates the timescales of the maximum likelihood estimate, and the shaded region indicates a 95% confidence interval. A lag time of 30 frames was chosen.

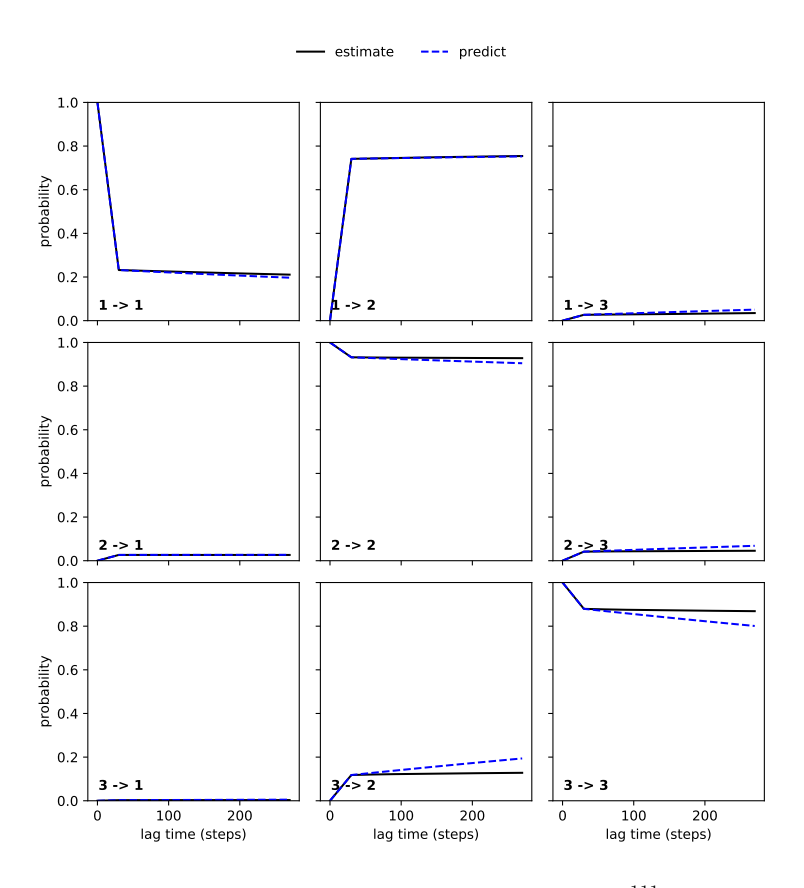


FIG. A14. Chapman-Kolmogorov test (3 macrostates) for a reversible Bayesian MSM^{111} constructed from the CGnet simulation data for chignolin. The dashed blue line is the prediction and black is the estimate.